The Effect of a Low Density Residuum on Geoid Anomalies and Topography

by

Mary Alexandra Agner

B.S., Physics
University of Southern Mississippi, 1996

Submitted to the Department of Earth, Atmospheric, and Planetary Sciences
in Partial Fulfillment of the Requirements for the Degree of
Master of Science in Earth and Planetary Sciences

at the

Massachusetts Institute of Technology

September 1998

Signature of Author.....
Department of Earth, Atmospheric, and Planetary Sciences
August 7, 1998

Certified by.....
Bradford H. Hager
Professor of Earth, Atmospheric, and Planetary Sciences
Thesis Supervisor

Accepted by.....
Ronald Prinn
Chairman, Department of Earth, Atmospheric, and Planetary Sciences

The Effect of a Low Density Residuum on Geoid Anomalies and Topography

by

Mary Alexandra Agner

Submitted to the Department of Earth, Atmospheric, and Planetary Sciences
on August 7, 1998, in Partial Fulfillment of the
Requirements for the Degree of Master of Science in
Earth and Planetary Sciences

ABSTRACT

Recent seismological measurements of the Pacific oceanic structure have detected a positive correspondence between surface topography, seismic wave speed, and the geoid (gravitational potential). High seismic wave speed indicates cold material sinking, which pulls the surface downward. Thus, topographic lows are expected to correlate with seismic wave speed highs, contrary to the new seismic measurements. We propose models which include two segregated materials, representing the fertile upper mantle and the residue from crustal melting, in order to decouple the surface topography from subsurface convection and create a positive correlation between topography and wave speed. We add a low viscosity zone beneath the residue to enhance the density contribution to the geoid anomaly and ensure that its sign is in phase with that of the surface topography and wave speed. Our models produce surface topography and geoid anomalies comparable to the recent seismological measurements. These models offer constraints on the strength of the low viscosity zone as well as the density difference between the residue and the upper mantle.

Thesis Supervisor: Bradford H. Hager
Title: Professor of Earth, Atmospheric, and Planetary Sciences

I. Introduction

Density anomalies within the interior of the Earth affect the gravitational potential, or geoid, at the surface. Geoid measurements can be used to quantify convection processes within the mantle of the Earth by relating the density anomalies caused by flow to the direction and orientation of the flow. Combining geoid observations with topography measurements relates surface features to convective processes. Including seismic data adds spatial resolution to the density anomalies, the motion that generates them, and their surface expressions.

Seismic studies of the Pacific oceanic structure between Tonga and Hawaii have found evidence that topography, geoid, and wave speed are all positively correlated (Katzman *et al.* in press). Katzman and coauthors find a sinusoidal pattern of seismic wave speed variations with a wavelength of 1500 km and an amplitude of 700 km. The topography and geoid associated with the seismic data also show the sinusoidal variation; the peaks and troughs of the topography, geoid, and seismic wave speed all occur simultaneously. The difference between peak and trough measurements in the geoid data is about 4 meters. The corresponding topography has a maximum at about one kilometer. Other studies of gravity and bathymetry have shown similar results in different areas of the Pacific (Cazenave *et al.* 1995). In this work, we explore a probable explanation for the cause of the positive correlation between topography, wave speed, and geoid anomaly.

The two general classifications of density anomalies are upwellings and downwellings. Subduction zones, where one plate is recycled by sliding under another, are examples of downwellings. Large expanses of volcanism like Hawaii are the surface

expression of upwellings. The concentration of mass in a downwelling will increase the geoid height at the surface, while the less dense upwelling will decrease the height of the geoid. This density anomaly would be the only contribution to the geoid if the boundaries between the different media, the crust and the air for instance, were constrained not to move. However, the deformation of the surface as it is pulled down by the downwelling and uplifted over the upwelling will affect the geoid (Richards and Hager 1984). Thus, two phenomena contribute to the geoid: density anomalies and the deformation of boundaries which separate layered materials of different density.

A simple box model exhibiting downwelling and upwelling is shown in the bottom panel of Figure 1. This model is an example of Rayleigh-Benard convection: two-dimensional convection maintained by fixed temperatures at the bottom (hot) and top (cold). The contour intervals (isotherms) and color shading indicate nondimensional temperature. The depth of the box is 670 kilometers, and in this model the thermal Rayleigh number, a dimensionless parameter discussed later in more depth, is 10^5. The sense of motion in the box, clock-wise, is shown by the velocity vectors. On the right side of the box, material is downwelling; on the left it is upwelling. This can also be seen in the isotherms: on the right side of the box they bend down, indicating that cold material is moving downwards. As the cold material on the right side sinks, it deforms the surface by pulling it downwards. Conversely, hot, buoyant material on the left side of the box exerts stresses to uplift the surface. The topography for this physical situation is shown in the middle panel of Figure 1. The nondimensional values used in the numerical calculations were transformed to real values by assuming a viscosity of 10^{21} Pascal seconds, that the

depth of the box is as given above, and the thermal diffusivity is 10^{-6} meters squared per second.

If we assume that the materials above and below the area represented by the box have different densities than the material within the box, then the top panel of Figure 1 illustrates the geoid anomaly for this convecting system. Figure 2 illustrates the components of the geoid anomaly: one for the density anomaly, one for the deforming lower surface, and one for the deforming upper surface. The density contribution is represented by the dashed line which rises from -4 meters to 4 meters, from upwelling to downwelling. The deformation of the top boundary decreases the amount of mass on the right side of the box, relative to a horizontal surface, by replacing the mass with air as the surface is pulled downwards, as seen in the heavy, dotted line in Figure 2. The bottom surface also deforms due to the increase of mass on the right side of the box, but its contribution to the surface falls off exponentially with depth, and so has a smaller value, represented by the upside-down triangles. Summing these three contributions produces the total geoid anomaly: the solid line in the figure. Both the total geoid and the topography agree well with previous work for a similar convecting system (Parsons and Daly 1983, see their Figure 11).

This relationship between downwelling cold material and lowered topography is supported by seismic data that shows high wave speeds (indicating cold material) in downwelling regions with depressed topography. For simple situations, then, we would expect low topography and high wave speeds at downwelling regions (Richards and Hager 1984); high topography and low wave speeds at upwellings. More concisely: the

topography and wave speed should correlate negatively with each other. The sign of the geoid for each situation is less strictly dictated. Previous work (e.g. Hager 1984) has shown that certain layered viscosity structures can reverse the sign of the geoid. We utilize this fact later in our model to achieve positive correlation between all three quantities.

The elevated topography in the data of Katzman and his co-workers could imply that an upwelling is lifting the surface. Or, the topographic high could be the result of material accumulating and raising the surface height. However, a high seismic wave speed implies the presence of cold material downwelling. Thus, the seismic and topographic data taken together seem to indicate downwellings beneath elevated terrain. Katzman and colleagues hypothesize that the residue produced in melting actively affects the topography near hot spots. During a melting event, the composition of the parent rock alters as the melt rises buoyantly. The residue which remains is neither melt nor undepleted mantle. The density of this residue is between crustal, or melt, values near 2700 kilograms per cubic meter and the density of the undepleted upper mantle, 3300 kilograms per cubic meter. This new density allows the residue to rise above the undepleted parent rock. The theory of Katzman *et al.* proposes that the residue between Tonga and Hawaii is transported by plate motion to the downwellings and left there to create the topographic high, and to stabilize the convecting rolls.

In this work, we examine the effect of such a residue on the positive correlation between topography, geoid, and wave speed by calculating geoid and topography for a layered system with contrasting viscosities.

II. Model

To model the behavior of the convecting system, the finite element code ConMan (King *et al.* 1990) was used to solve the equations of motion for infinite Reynolds number:

$$\tau_{ij,j}+f_i=0$$

and conservation of energy

$$(\frac{\partial}{\partial t}+u\cdot\nabla)T=\kappa\nabla^2T+A$$

with double diffusive convection

$$(\frac{\partial}{\partial t}+u\cdot\nabla)C=\frac{1}{Le}\nabla^2C$$

for an incompressible, Newtonian fluid in a square, two dimensional geometry. Rho is density, u the velocity vector, τ_{ij} is the stress tensor, f_i the body forces, A the internal heat sources, κ the thermal diffusivity, and C the composition function. The Lewis number, Le, is defined as the ratio of the thermal diffusivity to the chemical diffusivity. Qualitatively, the code takes an initial temperature distribution for the physical situation and calculates resulting velocities from that temperature distribution. Then that velocity field advects the temperatures and generates a new density distribution for the next velocity field calculation.

In reality, ConMan solves the nondimensional form of the momentum and energy equations. Once the nondimensional stress and temperature values have been calculated for the duration of the model run, we convert them to values with real units. In order to

do so, we use the definition of the thermal Raleigh number:

$$Ra = \rho g \alpha \Delta T d^3 / \kappa \eta$$

where ρ is the density of the medium in the box model, g is the gravitational acceleration, α is the thermal expansion coefficient, ΔT the temperature difference across the model box, d the depth of the box, κ the thermal diffusivity, and η the viscosity. The Rayleigh number is a unitless value that describes the vigor of the convection that occurs in a physical system. For each set of variables in the definition, there is a unique combination which produces the *critical Rayleigh number.* For a given system, values below the critical Rayleigh number do not convect.

To create temperature values in Kelvin, we multiply the nondimensional temperature, T', by the following factor, composed of terms in the Rayleigh number

$$T = (Ra\ \eta\kappa/\rho\alpha d^3)\ T'.$$

Similarly, stresses in Newtons per meter squared are calculated by

$$\sigma = (\eta\kappa/d^2)\ \sigma'.$$

We also include the effect of composition (Hansen and Yuen 1990) on the density of the model system by defining density

$$\rho = \rho_o\ (1 - \alpha T - \beta C)$$

where ρ_o is the average density of the upper mantle, α is the thermal expansion coefficient, β is the compositional expansion coefficient, T is the temperature, and C the composition function. The composition function accounts for the manner in which density is dependent on iron content and other physical properties. Primitive mantle material is represented by compositional values of C=1 and processed, melted material has compositional values of

C=0.

We use the temperature and stresses produced by ConMan to calculate geoid anomalies and topographies in the following manner: the density difference as a function of depth

$$\Delta\rho_n(z)=\frac{2}{L}\int\Delta\rho(x,z)\cos(\frac{2\pi nx}{L})dx$$

is calculated from the temperature and composition at every position in the model box. We solve Poisson's equation

$$\nabla^2 V=-4\pi G\rho$$

for the gravitational potential due to each row of density within the model

$$\delta V_n=-\frac{GL}{n}\int\Delta\rho_n(z)\exp(\frac{-2\pi nz}{L})dz$$

as a function of wavenumber and depth. Finally, we sum each of the potential terms to create the potential at the surface based on the thermal and compositional structure of the model:

$$\delta V(x)=\sum_{n=1}\delta V_n\cos(\frac{2\pi nx}{L})$$

The geoid anomaly is then related to the gravitational potential by

$$\delta N=\frac{\delta V}{g}.$$

To create the surface topography, we use the deviatoric stresses and pressures at the top

of the box

$$\sigma_{total}=\tau_{zz}-p_{zz}$$

to generate the total stress at the surface. The surface topography is then

$$h=\frac{\sigma_{total}}{(\rho_{air}-\rho_{mantle})g^2}.$$

This model can be viewed as motion within the cross section of a spreading ridge moving in time (Buck and Parmentier 1986). The convection in the lower layer represents Richter rolls. Richter rolls (Richter and Parsons 1975) are three dimensional effects caused by fast plate motion: as the plate moves over the mantle, it organizes the fluid into rolls whose long axes are parallel to the direction of plate motion. The path traced out by a given particle would be a spiral, simultaneously convecting up and down while being propelled forward by shear from the plate. Richter and Parsons (1975) proposed these "small scale" convection cells were on the order of 670 kilometers.

We choose the residue from some melting event to be the top dynamical layer of our two layer model, and the upper mantle (to a depth of 670 kilometers) to be the lower layer as shown in the top panel of Figure 3. We neglect the presence of the crust, because at and near the surface, it will be too cold and viscous to flow. In models with more than two layers, the residue is always the uppermost layer. Further, the residue and undepleted mantle are always kept from mixing, and are thus referred to as separate dynamical layers. Each of the dynamic layers may contain multiple layers with different viscosities as shown

in the bottom two panels of Figure 3.

We assume an oceanic crustal thickness of 6 kilometers and calculate from mass balance the amount of depleted mantle, or residue, beneath this crust. Typical melting percentages for mid-ocean ridges range from 8% to 20% (Klein and Langmuir 1987); the smaller number meaning that less melt is produced, and consequently more residue. Using the lower bound for the melting percentages, calculations for the thickness of the residue layer yield a value of approximately 67 kilometers. We vary the density difference between the residue and the undepleted mantle from 1% to 5% (based on discussion in Jordan 1979, Robinson 1988, and personal communication with Louise Kellogg). Within the model, this corresponds to compositional Rayleigh numbers

$$Ra_c = \rho g \beta \Delta C d^3 / \kappa \eta$$

of -10^5 and -5×10^5. This equation defines the compositional expansion coefficient, β.

Along all of the horizontal boundaries the vertical velocity is constrained to be zero, while on the vertical boundaries the horizontal velocity is constrained to be zero. One class of models contains an impermeable, horizontal boundary along which the vertical velocity is also zero. For each of the six "corners," the four corners of the entire box and the two points where the impermeable boundary meets the vertical sides of the box, both the horizontal and vertical velocities are zero. This form of layering is the simplest numerical model that separates residue and undepleted mantle, and we use it as our initial case. We also explore models that allow the boundary between residue and primitive mantle to deform.

The thermal Rayleigh number for each run is 10^5. The value for the Earth is a

controversial issue; most theoretical arguments conclude that the value is closer to 10^7 or 10^8. Using the thermal diffusivity value given above, an average density for the mantle of 3300 kg m^{-3}, a thermal expansion coefficient of $3x10^{-5}$ per Kelvin, a temperature difference of 1000 K, a viscosity of 10^{21} Pascal seconds, and choosing the depth of the model box to be 670 kilometers, the resultant Rayleigh number is 291800, showing that our assumed value is valid for these circumstances. These values are also those used to redimensionalize the temperatures and stresses. Since the temperature drop is better constrained than the viscosity, assuming a Rayleigh number of 10^5 and values for the other parameters given above, the viscosity for the system is $2.92x10^{21}$ Pascals.

There is no internal heating within the model; the temperature boundary conditions are constant temperature at the base and the surface (the Rayleigh-Benard conditions mentioned above). Likewise, the composition boundary values for those models which track composition are constant composition at base (1) and surface (0).

The simplest case includes the impermeable boundary mentioned above, which separates two layers of the same viscosity. The two layers interact along the segregating boundary. Cases where the viscosity of the upper layer, the residue, has a viscosity either 100 times or 0.01 times that of the residue provide interesting geoids and topography.

Both temperature and pressure profiles increase with depth within the Earth. As the temperature increases, the viscosity decreases. However, as the pressure increases, the viscosity increases. This results in a layer of low viscosity where temperature effects dominate; this phenomenon gives way to layers of increasing viscosity as the pressure effects take precedence. Thus, models with a layer of lower viscosity above layers with

larger viscosities are more likely to represent the physical characteristics of the upper mantle of the Earth. This layer is called the low viscosity zone and resides below the base of the residue. Rock mechanics experimentation and geophysical modeling give evidence for this phenomenon. We emphasize that it is only through this method of layering that we introduce viscosity contrast within our models; viscosity is never temperature dependent, only depth dependent.

We explore the effects of a low viscosity zone by adding a layer of lower viscosity to the models with $\eta_{upper}/\eta_{lower} = 100$. These sub-cases containing the low viscosity zone are all comprised of an upper layer with viscosity 10^{21} Pascal seconds, and a lower dynamic layer which is further divided into either three or four portions with different viscosities, see lower panels in Figure 3. Because the extent of the low viscosity zone is contested, the sub-layers within the bottom dynamical layer have different thicknesses as well as number.

Finally, we increase the realism in the model by removing the horizontal, impermeable boundary. Instead, the residue and the undepleted mantle were distinguished by different values of the composition function. Thus, the transportation and entrainment of the residue within the pristine mantle can be viewed. We concentrate our discussion and applications on those models with both a free boundary between the upper mantle and the residue and a low viscosity zone.

III-a. Results with An Impermeable Boundary

For the case with two layers of the same viscosity, with 10% of the model above the impermeable boundary, shown in the bottom panel of Figure 4, the small upper layer exhibited a single cell of convection. The velocities of the upper cell are much smaller than those of the lower cell; examination of the temperature contours indicates that the motion in the upper layer is a result of driving from the shear stresses exerted by the thermally convecting bottom layer.

The total geoid for the system ranges from about 2 meters above a reference level over the upwelling to 2 meters below, over the downwelling. See top panel of Figure 4. For the two layer system, there are 4 contributions to the geoid: the deformation of the surface topography, that of the internal boundary, and a density contribution from each layer. Examining this panel shows that this geoid is smaller than the case without the internal boundary. This occurs because the contribution from the topography on the internal boundary dwarfs all the other contributions. The upper layer, which is circulating in the opposite sense to the lower layer is uplifted slightly at the right side of the box, in order to contribute in the same direction as the density anomaly from the lower layer.

The total geoid correlates negatively with the surface topography because the surface topography is positive above the downwelling occurring in the lower layer, as seen in the center panel of Figure 4. This happens because the counter-clock-wise circulation induced in the upper layer has an upwelling on the right side of the box.

Clearly defined cells exist in the upper layer (the 10% of the model above the impermeable boundary) of the system with viscosity contrast $\eta_{upper}/\eta_{lower} = 0.01$. See the

lower panel of Figure 5. These complete cells are approximately 150 kilometers in width. The right-most cell is somewhat time dependent. This cell occurs over the downwelling of the lower layer, and appears most strongly when the upwelling of the smaller cell occurs in phase with the downwelling of the lower layer. Since the overturn time for the upper layer is greater than the lower layer, the dissonance between the two produces instabilities within the upper layer which propagate toward the complete cells, disrupting the cell just to the left of the time dependent one. The regularity of the cells closest to the upwelling dissipates the instability that propagates from right to left.

The geoid and surface topography for the 0.01 case shown in Figure 5 do not exhibit signs of the small convection cells within the upper layer. The deformation of the surface creates a geoid low above the downwelling of the lower layer, and so the surface topography and geoid are not positively correlated. The geoid also exhibits a time dependence, which appears secular. At earlier stages of the model run, the geoid is positive above the downwelling. Later, it changes to become negative above the downwelling.

The two layer case with viscosity ratio 100 looks very similar to the case with two layers of the same viscosity; compare Figures 4 and 6. The geoid is negative over the downwelling and slightly smaller, having an amplitude of 1.5 meters. The topography is high above the downwelling in the lower layer, and has a maximum of about 300 meters, which is larger than the viscosity ratio 1 case.

III-b. Results With Free Boundary and Low Viscosity Zone

Geophysical modeling and other data indicate that the viscosity of the upper mantle is not constant, as assumed in the previous models. There is a layer of lower viscosity beneath the crust and residue (Hager 1984, Davies and Richards 1992). Because the upper layer in our model is most likely to be cold and dry (it is near the surface and the water within it has been removed by melting), we choose to examine the effect of a low viscosity zone on the geoid for the system with a viscosity contrast of 100. To vary the viscosity in the lower portion with depth we include a layer below the conducting lid whose viscosity is 1000 times smaller than that of the lid. In the models containing four different layers of viscosity, the layer directly below the residue has a viscosity of 10^{20} Pascal seconds, the third layer has a viscosity one hundredth that value and represents the low viscosity zone, and the lowest layer the same viscosity as the second layer. In the models with only three layers, the layer directly below the residue has a viscosity of 10^{18} Pascal seconds, and the bottom layer a viscosity of 10^{20} Pascal seconds. Schematics of the viscosity structures for both types of models are shown in Figure 3.

The most simple model with the low viscosity zone is one that allows the rest of the model (the portion remaining after the residue layer and the low viscosity zone) to be isoviscous. The density difference between the two materials is 1%. Because some petrological data suggest that the density change incurred by melting could be smaller than 2% (Jordan 1979) this approximation is valid. First, we took the thickness of the low viscosity zone to be the same as the residue. These circumstances, shown in Figure 7, denoted 10-10-80 for the percentage thickness of each layer, produce a positive geoid

above the downwelling. This geoid has a maximum of 8 meters, and can be seen in the upper panel of the figure. The bottom panel of the figure has nondimensional temperature demarcated by the contour lines and composition indicated by the color shading. This representation scheme holds for all figures of similar content. This figure also displays the entrainment of the residue layer, illustrated by the blue material sinking into the red. Changing the thickness of the low viscosity zone to twice that of the residue doesn't appreciably change the amplitude of the geoid. This viscosity structure is denoted 10-20-70, meaning that the upper 10% of the model has a viscosity of 10^{21} Pascal seconds, the middle 20% a viscosity of 10^{18} Pascal seconds, and the lower 70% a viscosity of 10^{20} Pascal seconds. This is depicted in the bottom portion of Figure 8. The geoid remains positive above the downwelling. The surface topography rises to approximately 600 meters above the downwelling in both cases. The small hump near the upwelling in the topography seen in the 10-10-80 case also appears in the 10-20-70 case, see center panel in Figure 8.

Increasing the thickness of the low viscosity zone to be the majority of the lower layer, as in case 10-80-10, shown in Figure 9, increases the amplitude of the geoid and topography. The sign of the topography and geoid remain the same, positive above the downwelling. The topographic hump seen in the 10-10-80 and 10-20-70 cases smooths over in 10-80-10 case.

Within the finite element calculations, the compositions of the residue and the mantle diffuse, so that while the primitive mantle (1) and residue (0) continue to exist, material forms with fractional composition values. All previous geoid calculations were

based on rounding such fractional compositions to integer values. Figure 10 shows the 10-20-70 case where the geoid anomaly has been calculated using the fractional composition values; compare it with Figure 8. There is no discernible difference between the two geoids and surface topographies.

A 5% density difference between the residue and the remaining material decreases the amount of entrainment for the 10-20-70 viscosity structure, but does not reverse the sign of the geoid: it stays positive above the downwelling. The amplitude of the geoid increases, now rising 200 meters above the reference level as seen in the top section of Figure 11. The topographic maximum rises to 20 kilometers. The topographic hump noted in the 10-20-70 case with 1% density difference has diminished but remains slightly visible.

Next, we looked at the effect of separating the low viscosity zone from the residue by inserting a layer of intermediate viscosity. The 10-10-70-10 case, shown in Figure 12, exhibits much less entrainment than the 10-70-10-10 case in Figure 13. The 10-10-70-10 case has the upper 10% of the model with a viscosity of 10^{21} Pascal seconds, the next 10% has a viscosity of 10^{20} Pascal seconds, the 70% a viscosity of 10^{18} Pascal seconds, and the remaining 10% a viscosity of 10^{20} Pascal seconds. Both produce positive geoid anomalies above the downwelling of the model, seen in the top panels of Figures 12 and 13, with maxima at about 6 meters. The surface topography is also similar, with a maximum at about 500 meters. Again, the effect of integer or fractional composition values can be neglected, as shown by comparison of the fractional geoid and topography in Figure 13 with that of the integer composition case of 10-70-10-10 displayed in Figure 14.

Figure 15 illustrates the 10-70-10-10 case with 5% density difference between mantle and residue. The main difference between the 10-70-10-10 case with a density difference of 1% and that with a 5% density difference occurs in the geoid. The topography for the case with 5% density difference is larger than in the 1% case, but not by the magnitude of the geoid anomaly. Examining the temperature and composition contours for both the 1% and 5% cases of 10-70-10-10 shows that the temperature contours are fairly similar. However, the amount of entrainment increases greatly with the 1% case. Thus, the compositional structure of the model affects the geoid more than the thermal profile. This can also be seen in Figure 16, which shows the geoid contribution from density which is a function of both temperature and composition (dot-dash line) and the geoid contribution from density which is a function of temperature only (triangles).

For a given density difference, the composition profile depends on the viscosity structure, so in the end the viscosity structure dictates the geoid. For those cases with the low viscosity zone abutting the residue, the amount of entrainment is small; see Figure 12. Both the viscosity structure and the density difference between the residue and the fertile mantle limit the amount of entrainment, and the amount of entrainment determines the amplitude of the geoid.

IV. Discussion

Satellite data in the Pacific (Haxby and Wessel 1986, Weissel *et al.* 1994, Cazenave *et al.* 1995) exhibit three somewhat distinct ranges of topography and geoid wavelengths: less than 200 km, between 400 and 600 km, and greater than 1000 km. These features have geoid values in the tens of centimeters (Cazenave *et al.* 1995). Early studies of the Pacific (Watts *et al.* 1985) found a positive correlation between geoid anomalies and bathymetry. They conclude that dynamic compensation is creating the correlation. Dynamic compensation occurs when surface topography is the result of convective processes rather than lengthening or shortening of lithospheric material. This work upholds that conclusion, assuming that a low viscosity zone exists between the residue and 670 kilometers depth. However, many of the measured geoid anomalies in the Pacific have average amplitudes of, at most, a few meters. The majority of geoids in this study range from 6 to 20 meters.

The wavelength for the geoid and topography modeled in this work is 670 kilometers, close enough to 1000 kilometers that results from the Cazenave study (Cazenave *et al.* 1995) at that wavelength are applicable. Cazenave and her colleagues examine the geoid to surface topography ratio, called the admittance, of the central Pacific. Admittance can often be used to differentiate between processes which create geoid anomalies and surface topography. They calculate a low admittance value, leading them to conclude that the origin of the processes creating the centimeter-sized geoid is within the lithosphere. They caution that this does not discount convection as a method to generate the geoids measured in the central Pacific. The admittance calculated for the

models in this study is roughly 10 meters per kilometer. This value is higher than that of Cazenave *et al.* (1995), but not sufficiently different to preclude convection as the process making the geoid and topography.

While other studies have looked at the effect of the partial melt residue on topography and gravity, most have done so without including a low viscosity zone. Robinson (1988) found that the density contribution to the geoid is larger than the topography contribution for her model of volcanic swells. The presence of a low viscosity zone in our models results in the reverse: the contribution of the surface topography dwarfs the density contribution. Figure 16 shows the total density contribution, the dot-dash line, the surface topography contribution, the dotted line, and the density contribution dependent only on temperature, the triangles, for the 10-20-70 case with a 1% difference in density, equivalent to the 0.7% density difference used in the Robinson (1988) models. Such conflicting results imply that the low viscosity zone enhances the effect of the density contribution to the geoid enough to alter the sign of the total geoid.

The models of Robinson *et al.* (1987) which do include a low viscosity zone examine its effect on compensation depth. They find that the presence of the low viscosity zone causes the geoid and topography to change sign. This study confirms their findings: the low viscosity zone enables our models to yield a positive geoid above a downwelling.

Measurements of volcanic ridges in the Pacific have been used in support of boudinage as the explanation for the gravity and topography lineations (Sandwell *et al.* 1995), rather than convection. Boudinage is a term that refers to the bunching and thinning of a layer of material due to extension. Sandwell *et al.* explain the measurements

by predicting the direction of stresses measured on the sea floor and can account for the change in direction of the gravity field due to a change in plate motion in the area of their study (the Pukapuka ridge). They dismiss small scale convection because it does not give volcanism in a gravitational low. The model proposed in this paper does: a geoid low corresponds to an upwelling in the upper dynamic layer. Another reason they reject small scale convection as a mechanism for the lineations in the Pacific is that it produces compressional stresses at gravitational troughs rather than gravitational crests. The upwelling in the upper dynamic layer of this model would produce a compressive stress at the geoid high, associating compressional stresses and gravitational highs as they require.

Their last criticism of small scale convection is that it has been shown to be too time dependent (Buck and Parmentier 1986): the presence of a change in plate motion remains in the gravity output of the small scale convection model, but is not present in the observations. This issue is not addressed in this paper because we assume steady state for each of the systems discussed above. While we cannot totally discount boudinage as the cause of the undulations in the Pacific, we can strengthen the case for the smaller-scale convection of our model because, with the inclusion of a low density residue and a low viscosity zone, it produces the observables.

In addition to neglecting the time dependence, and thus the cooling and thickening of the lithosphere, we have not included the effects of temperature dependent viscosity. The emphasis of these models is to examine the effect of the low density residuum. Depth dependent viscosity is more important than temperature dependence for this purpose. The effects of temperature dependent viscosity are unlikely to be large enough to reverse the

sign of the geoid by altering the density contribution to the geoid. Only by enlarging the topographic contribution to the geoid at the expense of the density contribution could temperature dependent viscosity exchange the geoid maxima and minima. Finally, temperature dependent viscosity should not change the sign of the surface topography and undo the decoupling work of the residue.

What measurements can be made to test the validity of these models? Could seismic data be used to map the deformation of the residue layer? The largest amount of deformation of the free boundary occurs in the 10-70-10-10 case with no density difference. The boundary is lowered by 200 kilometers at the downwelling. All other cases show at most tens of kilometers of entrainment. The average amount of entrainment, then, is small, and so provides no means with which to test these models.

While this model does not generate geoid and topography values identical to those measured in the Pacific, it does produce geoids on the same distance scale as the Pacific (Yamaji 1992) which correlate positively with surface topography and seismic velocity (Katzman *et al.* in press) by assuming a segregated lid of high viscosity above an upper mantle which contains a layer of low viscosity.

V. Conclusions

The most important aspect of this work shows that the residue created during the formation of oceanic crust decouples the surface topography from the internal convection. By accounting for this residue, our models provide a process linking the complex system of ridges and troughs found in the Pacific oceanic structure with their seismic wave signature. While the lower layer convects, the residue accumulates over the downwelling, making the surface topography the mirror image of the boundary between the two dynamic layers, as opposed to its twin.

Each model was used to calculate two values of geoid and topography to determine the sensitivity of density to integer or fractional values of the composition function. In one group, the fractional composition values resulting from diffusion during the numerical calculations were used to calculate density for the geoid and topography. In the other, all values of composition less than 0.55 were rounded down to 0, and the rest rounded up to 1. Then, geoid and topography were calculated again based on the new integer derived density. No difference was found between the two resulting geoids or surface topographies. The similarities in topography and geoid anomaly can be seen by comparing Figures 8 and 10, and Figures 13 and 14.

Additionally, these models emphasize the effect of a low viscosity zone on surface geoid measurements. By including a layer with markedly lower viscosity, the sign of the geoid may be reversed from the result obtained from mass balance reasoning. Without the layer of lowered viscosity, the sign of the geoid over the downwelling is negative. Figure 6 shows the two layer case with a viscous, residue lid and negative geoid over the

downwelling. A positive geoid can be created in the same situation (10-20-70) by the addition of a low viscosity zone (Figure 8).

Since each of the free surface models produces a positive surface topography and a positive geoid above the downwelling in the lower dynamic layer, our models cannot say more about the nature of the low viscosity zone than that its presence is necessary to explain the Katzman *et al.* data by convection. If the range of thicknesses included some geoid lows over the downwelling, than we could use these models to restrict the size of the low viscosity zone.

The key to producing sinusoidal geoid anomalies and topography with the near 1000 kilometers wavelengths measured in the Pacific is to utilize the aspect ratio one quality of convective rolls. We chose to extend our models only to a depth of 670 kilometers, including only the upper mantle for simplicity. This choice resulted in phenomena on the correct scale. From this, we deduce that some change occurs at approximately that depth, inhibiting convection. We suggest that an increase in the viscosity of the interior is responsible, and that such stratification may play a larger role in surface expressions than previously thought.

Our more complex models produce topography and geoid anomalies similar to the measurements of the Pacific oceanic crust. Seismic data beneath the Pacific (Katzman *et al.* in press) require that the surface topography and the geoid have highs that coincide with seismic wave speed highs. Simultaneously topographic highs and seismic highs imply a downwelling beneath a swell. This is explained in our models by the decoupling of topography and the density anomaly which dominates the geoid. The motion of the upper

dynamic layer produces the positive topography over the downwelling in the lower dynamic layer. The low viscosity zone generates a positive geoid above the same downwelling. These two effects taken together give the positive correlation between seismic wave speed, topography, and geoid measured in the Pacific.

References

Buck, W. R., E. M. Parmentier, Convection Beneath Young Oceanic Lithosphere: Implications for Thermal Structure and Gravity, *Journal of Geophysical Research*, **91**, 1961-1974, 1986.

Cazenave, A., B. Parsons, P. Calcagno, Geoid Lineations of 1000 Km Wavelength over the Central Pacific, *Geophysical Research Letters*, **22**, 97-100, 1995.

Davies, G. F., M. A. Richards, Mantle Convection, *Journal of Geology*, **100**, 152-206, 1992.

Hager, B. H., Subducted Slabs and the Geoid: Constraints on Mantle Rheology and Flow, *Journal of Geophysical Research*, **89**, 6003-6015, 1984.

Hansen, U., D. A. Yuen, Nonlinear Physics of Double-Diffusive Convection in Geological Systems, *Earth-Science Reviews*, **29**, 385-399, 1990.

Haxby, W. F., J. K. Weissel, Evidence for Small-Scale Mantle Convection from Seasat Altimeter Data, *Journal of Geophysical Research*, **91**, 3507-3520, 1986.

Jordan, T. H., Mineralogies, Densities, and Seismic Velocities of Garnet Lherzolites and Their Geophysical Entities, *The Mantle Sample: Inclusions in Kimberlites and Other Volcanics*, F. R. Boyd and H. O. A. Meyer, editors, American Geophysical Union, Washington D.C., 1979.

Katzman, R., L. Zhao, T. H. Jordan, High-Resolution, 2D Vertical Tomography of the Central-Pacific Mantle Using *ScS* Reverberations and Frequency-Dependent Travel Times, *Journal of Geophysical Research*, submitted.

King, S. D., A. Raefsky, B. H. Hager, ConMan: Vectorizing a Finite Element Code for Incompressible Two-Dimensional Convection in the Earth's Mantle, *Physics of the Earth and Planetary Interiors*, **59**, 195-207, 1990.

Klein, E. M., C. H. Langmuir, Global Correlations of Ocean Ridge Basalt Chemistry with Axial Depth and Crustal Thickness, *Journal of Geophysical Research*, **92**, 8089-8115, 1987.

Neumann, G. A., M. T. Zuber, Diffuse Extension and Lithospheric Boudinage, *Journal of Geophysical Research*, submitted.

Parsons, B., S. Daly, The Relationship between Surface Topography, Gravity Anomalies, and Temperature Structure of Convection, *Journal of Geophysical Research*, **88**, 1129-1144, 1983.

Phipps Morgan, J., W. J. Morgan, E. Price, Hotspot Melting Generates Both Hotspot Volcanism and a Hotspot Swell, *Journal of Geophysical Research*, **100**, 8045-8062, 1995.

Ricard, Y., C. Froidevaux, Stretching Instabilities and Lithospheric Boudinage, *Journal of Geophysical Research*, **91**, 8314-8324, 1986.

Richards, M. A., B. H. Hager, Geoid Anomalies in a Dynamic Earth, *Journal of Geophysical Research*, **89**, 5987-6002, 1984.

Robinson, E. M., B. Parsons, S. F. Daly, The Effect of a Shallow Low Viscosity Zone on the Apparent Compensation of Mid-Plate Swells, *Earth and Planetary Science Letters*, **100**, 335-348, 1987

Robinson, E. M., The Topographic and Gravitational Expression of Density Anomalies Due to Melt Extraction in the Uppermost Oceanic Mantle, *Earth and Planetary Science Letters*, **90**, 221-228, 1988

Sandwell, D. T., E.L. Winterer, J. Mammerickx, R. Duncan, M. A. Lynch, D. A. Levitt, C. L. Johnson, Evidence for Diffuse Extension of the Pacific plate from Pukapuka Ridges and Cross-Grain Gravity Lineations, *Journal of Geophysical Research*, **100**, 15,087-15,099, 1995.

Watson, S., D. McKenzie, Melt Generation by Plumes: a Study of Hawaiian Volcanism, *Journal of Petrology*, **32**, 501-537, 1991.

Watts, A. B., D. P. McKenzie, B. E. Parsons, M. Roufosse, The Relationship between Gravity and Bathymetry in the Pacific Ocean, *Geophysical Journal of the Royal Astronomical Society*, **83**, 263-298, 1985.

Wessel, P., D. Bercovici, L. W. Kroenke, The Possible Reflection of Mantle Discontinuities in Pacific Geoid and Bathymetry, *Geophysical Research Letters*, **21**, 1943-1946, 1994.

Yamaji, A., Periodic Hotspot Distribution and Small Scale Convection in the Upper Mantle, *Earth and Planetary Science Letters*, **109**, 107-116, 1992.

Yuen, D. A., L. Fleitout, Stability of the Oceanic Lithosphere with Variable Viscosity: an Initial-Value Approach, *Physics of the Earth and Planetary Interiors*, **34**, 173-185, 1984.

Figure Captions

Figure 1. Thermal structure, geoid anomaly, and surface topography for Rayleigh-Benard convection in a square box at steady state.

Figure 2. Density anomaly, surface topography, and internal boundary contributions to the geoid anomaly for the case of Rayleigh-Benard convection at steady state. The dotted line represents the surface topography component, the dashed line the density anomaly component, and the triangles the contribution due to the lower boundary. The solid line is the sum of all the components.

Figure 3. Schematics detailing the viscous and dynamic sections for the models discussed within the text. The dynamical layers delineate the impermeable or free boundary. The top box shows the case with the impermeable boundary positioned between viscosity 1 and viscosity 2. The middle panel shows the set of models with a free boundary between viscosity 1 and viscosity 2, and a low viscosity zone represented by viscosity 3. The bottom panel illustrates the viscosity structure for models with a free boundary between viscosity 1 and viscosity 2, and a low viscosity zone represented by viscosity 2.

Figure 4. Thermal structure, topography, and geoid for the case with an impermeable boundary separating two layers of the same viscosity.

Figure 5. Topography, geoid, and thermal structure for the model with an impermeable boundary separating the upper layer of low viscosity (10^{19} Pascal seconds) and the lower layer of higher viscosity (10^{21} Pascal seconds).

Figure 6. Geoid, topography, and thermal structure for the model with an impermeable boundary separating the upper layer of high viscosity (10^{21} Pascal seconds) and the bottom layer of lower viscosity (10^{19} Pascal seconds).

Figure 7. Composition, thermal structure, geoid, and surface topography for the model with a free boundary separating the highly viscous residue from a low viscosity zone (middle) and a layer of intermediate viscosity. The geoid derives from integer composition values, as shown in the bottom panel: blue represents residue and red the fertile upper mantle. The contour lines in the bottom panel represent temperature. The density difference between residue and mantle is 1%.

Figure 8. Topography, composition, thermal structure, and geoid for the three layer model with a free boundary separating the residue from a low viscosity zone twice its thickness. The geoid anomaly derives from integer composition values. The difference in density between the fertile mantle and the residue is 1%.

Figure 9. Geoid anomaly, topography, thermal structure, and composition for the three layer model with a free boundary separating the residue from a large (80%) low viscosity zone. The

difference in density between the residue and the upper mantle is 1%. The geoid anomaly is calculated from integer values of composition.

Figure 10. Topography, composition, thermal structure, and geoid for the three layer model with a free boundary separating the residue from a low viscosity zone twice its thickness. The geoid anomaly derives from fractional composition values. There is a 1% density difference between mantle and residue.

Figure 11. Topography, composition, thermal structure, and geoid for the three layer model with a free boundary separating the residue from a low viscosity zone twice its thickness. The geoid anomaly is calculated from integer composition values. The difference in density between residue and fertile upper mantle is 5%.

Figure 12. Geoid anomaly, topography, composition, and thermal structure for the 4 layer case with a thick low viscosity zone (70%) separated from the residue by a free boundary. Fractional compositional values are used to calculate the geoid anomaly. The density difference between the upper mantle and the residue is 1%.

Figure 13. Composition, thermal structure, topography, and geoid anomaly for the 4 layer case with a thick intermediate-viscosity layer between the residue and the low viscosity zone. A free boundary separates the intermediate layer and the residue. Fractional composition values were used to calculate the geoid anomaly. The difference in density between the residue and the mantle is 1%.

Figure 14. Composition, thermal structure, topography, and geoid anomaly for the 4 layer case with a thick intermediate-viscosity layer between the residue and the low viscosity zone. A free boundary separates the intermediate layer and the residue. The geoid anomaly is calculated from integer composition values. There is a 1% density difference between the viscous residue and the primitive mantle.

Figure 15. Composition, thermal structure, geoid anomaly, and topography for the 4 layer case with a thick intermediate-viscosity layer between the low viscosity zone and the residue. A free boundary separates the residue and the intermediate layer. The geoid anomaly is calculated from fractional composition values. The density difference between residue and fertile mantle is 5%.

Figure 16. The geoid anomaly contributions from the 10-20-70 model with a 1% density difference between mantle and residue. The dotted line represents the surface topography component, the dot-dash line is the total density component, and the triangles are the density contribution for density solely a function of temperature.

Figure #1 – Geoid

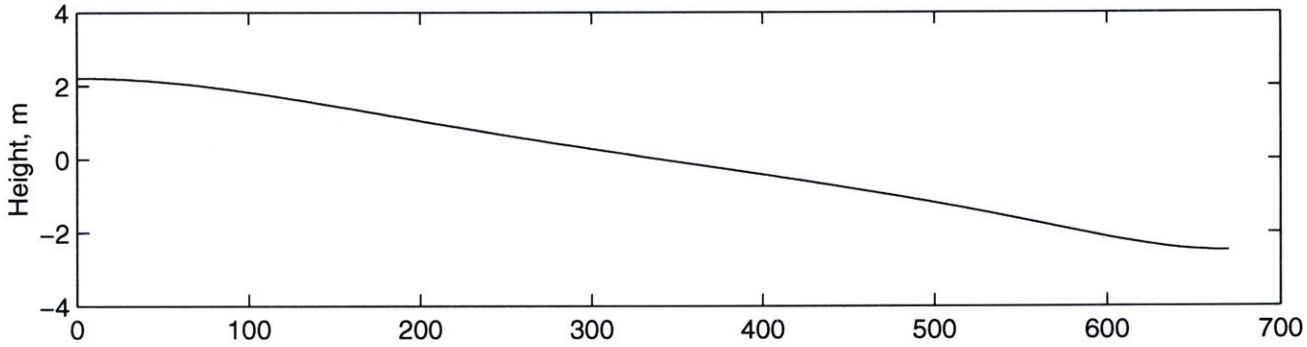

Topography

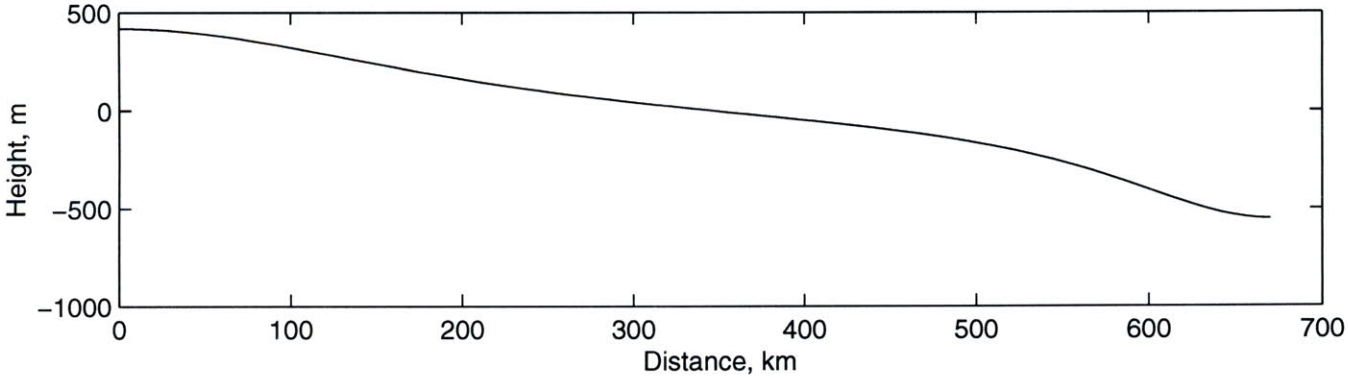

Rayleigh–Benard Convection

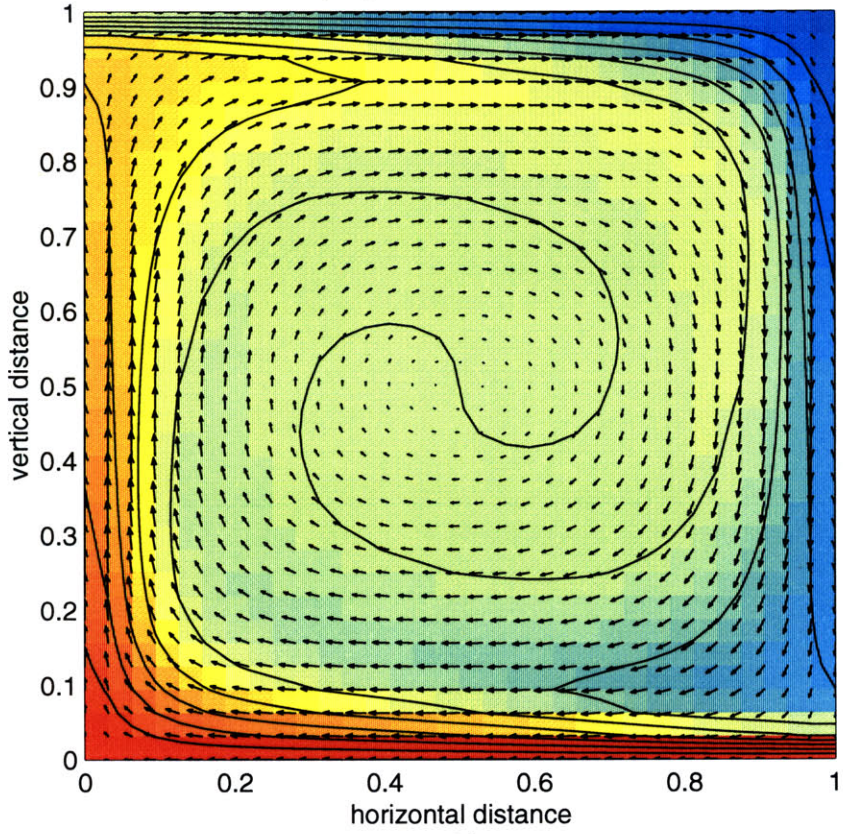

Figure #2 – Geoid Contributions in Rayleigh Benard Convection

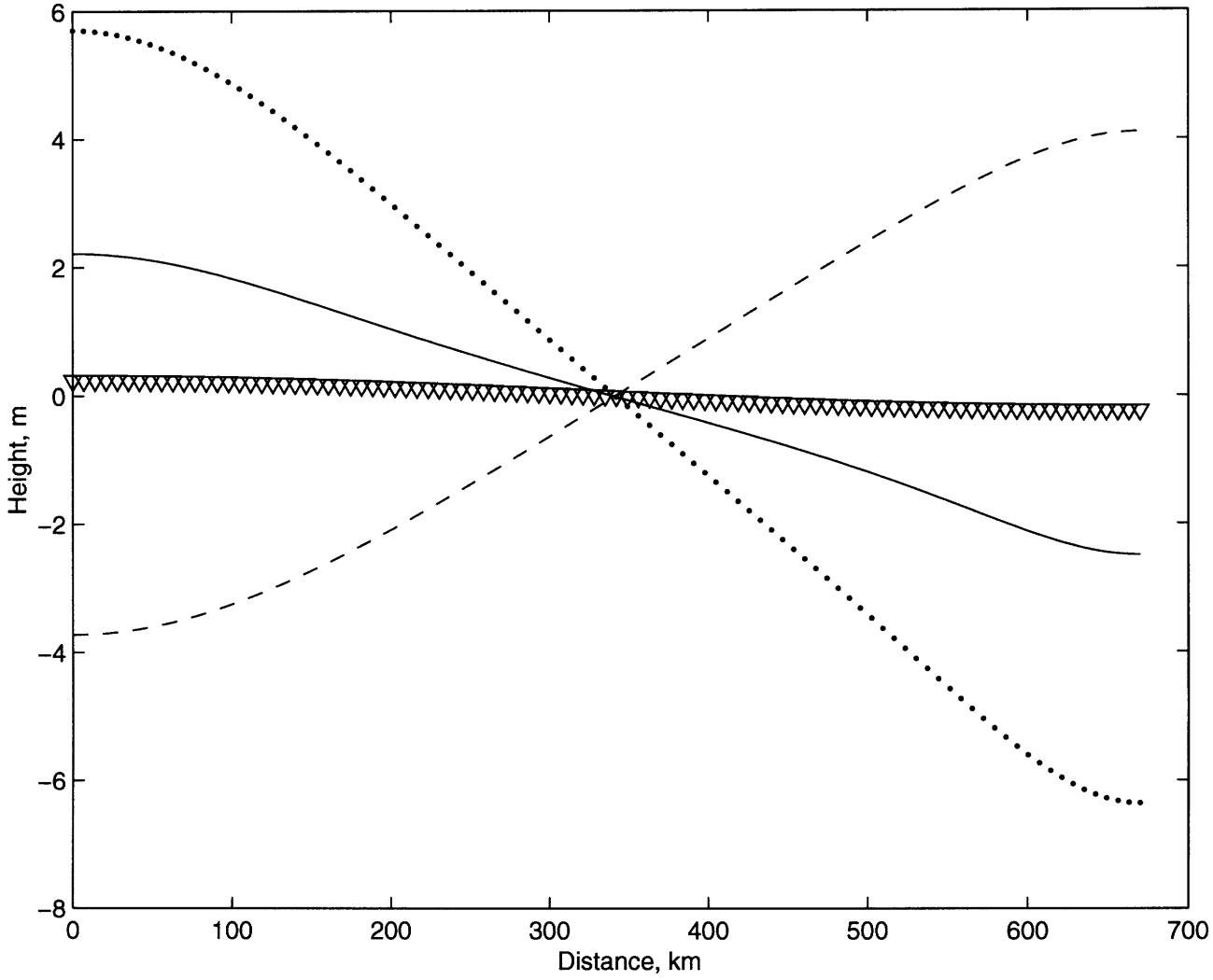

Figure #3

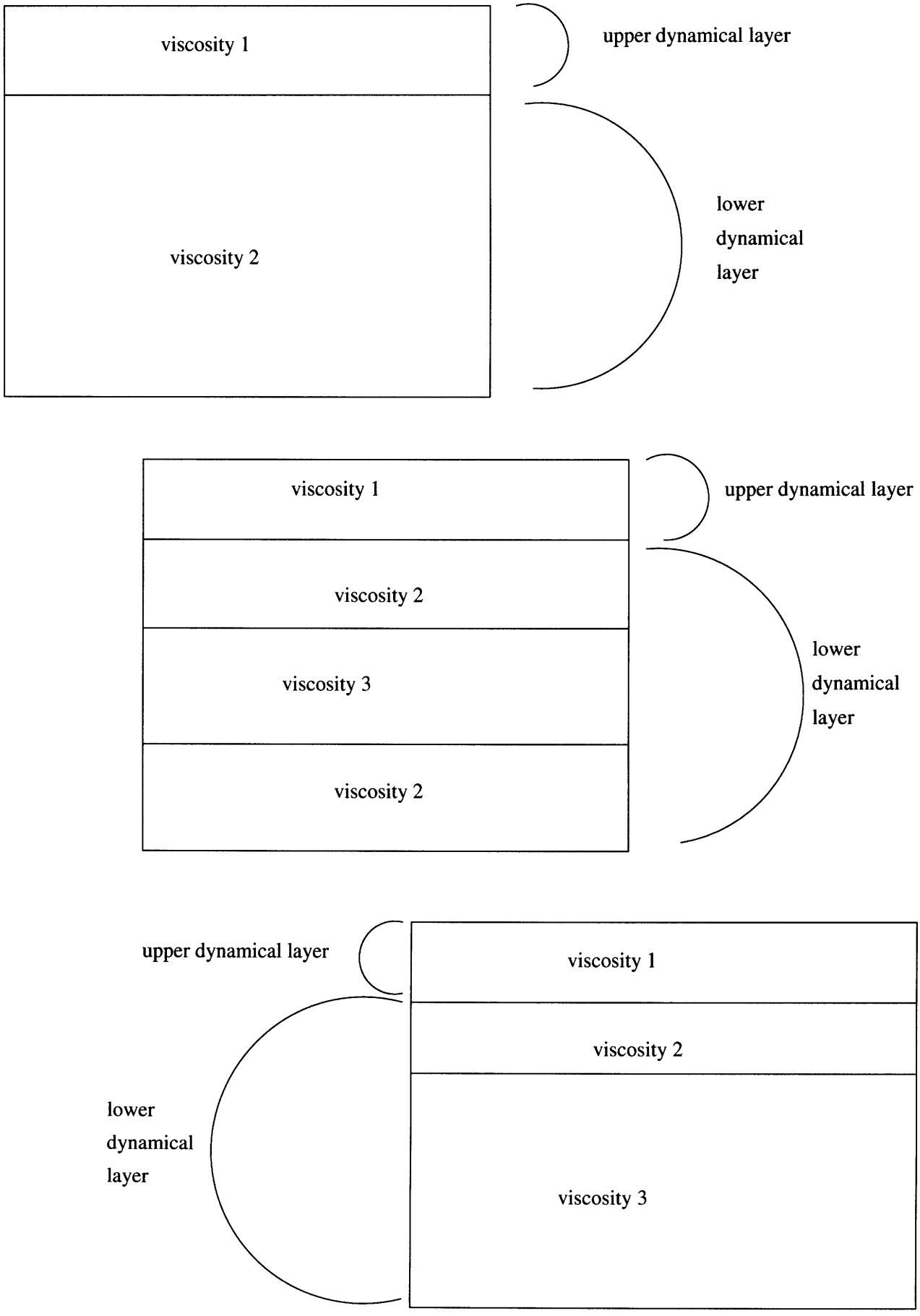
viscosity 1
viscosity 2
upper dynamical layer
lower dynamical layer
viscosity 1
viscosity 2
viscosity 3
viscosity 2
upper dynamical layer
lower dynamical layer
upper dynamical layer
viscosity 1
viscosity 2
viscosity 3
lower dynamical layer

Figure #4 – Geoid

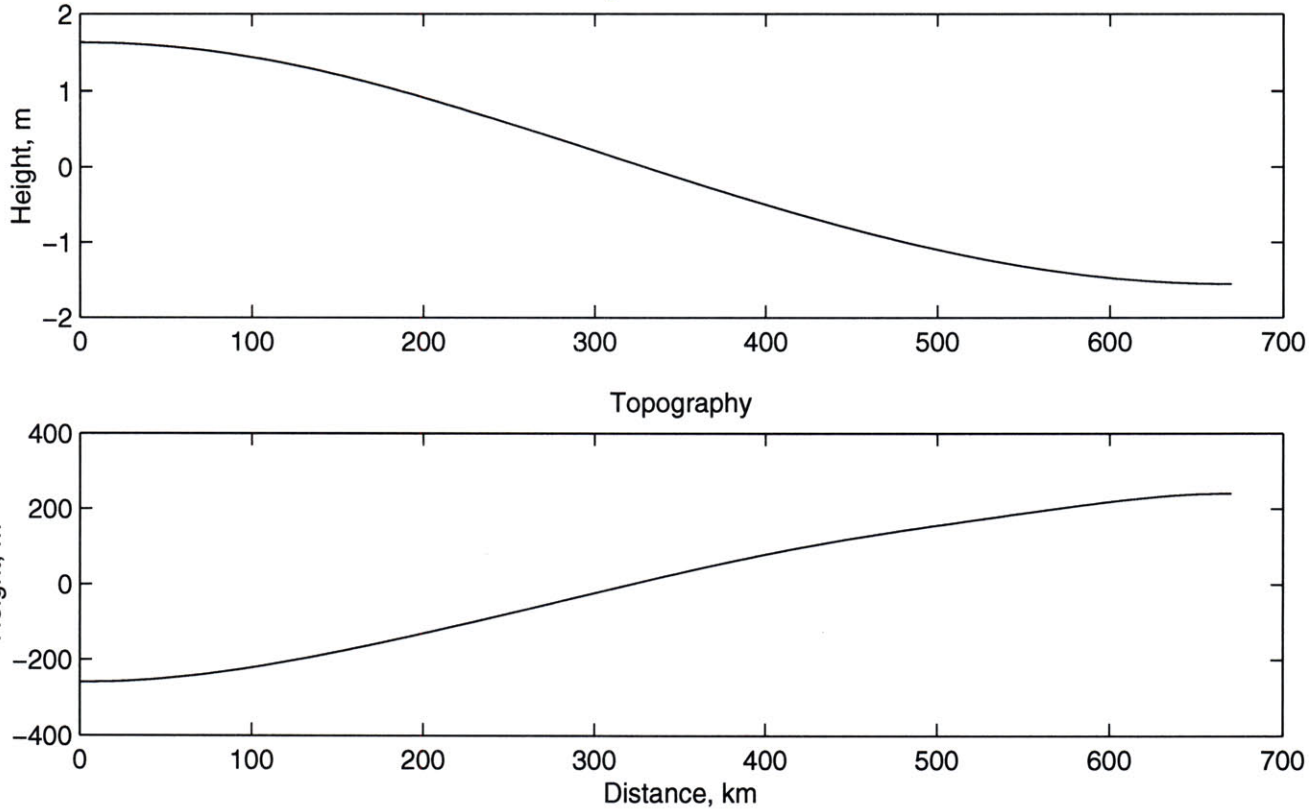

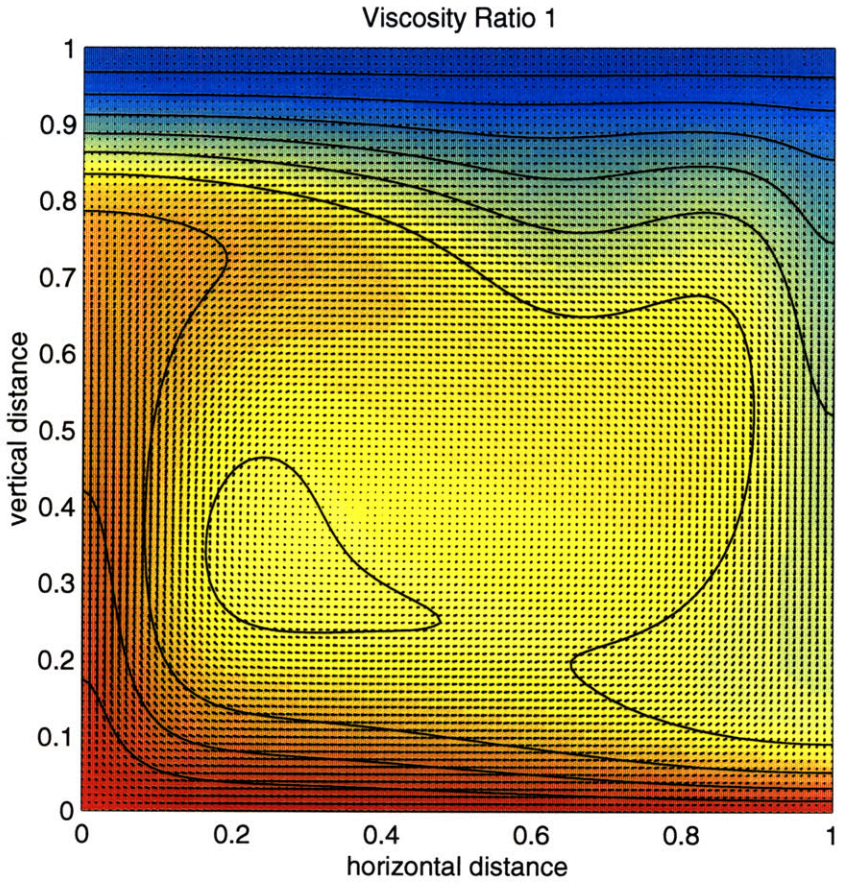

Figure #5 – Geoid

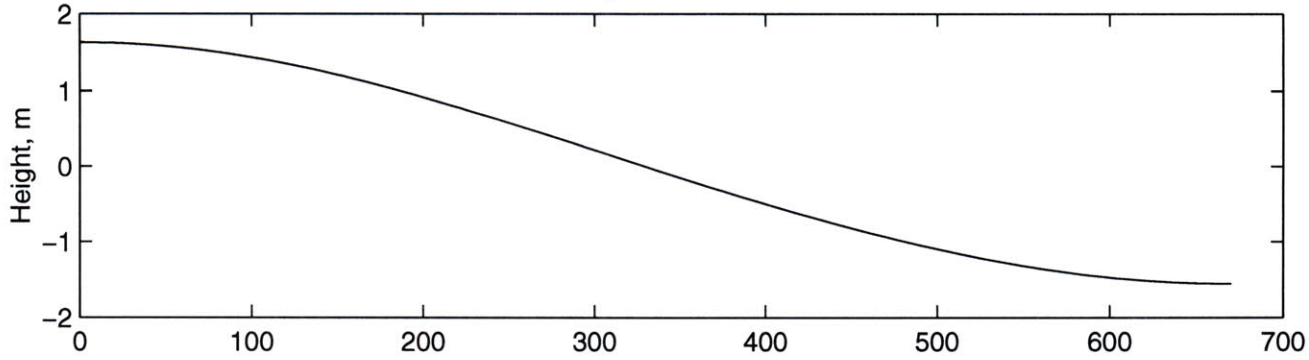

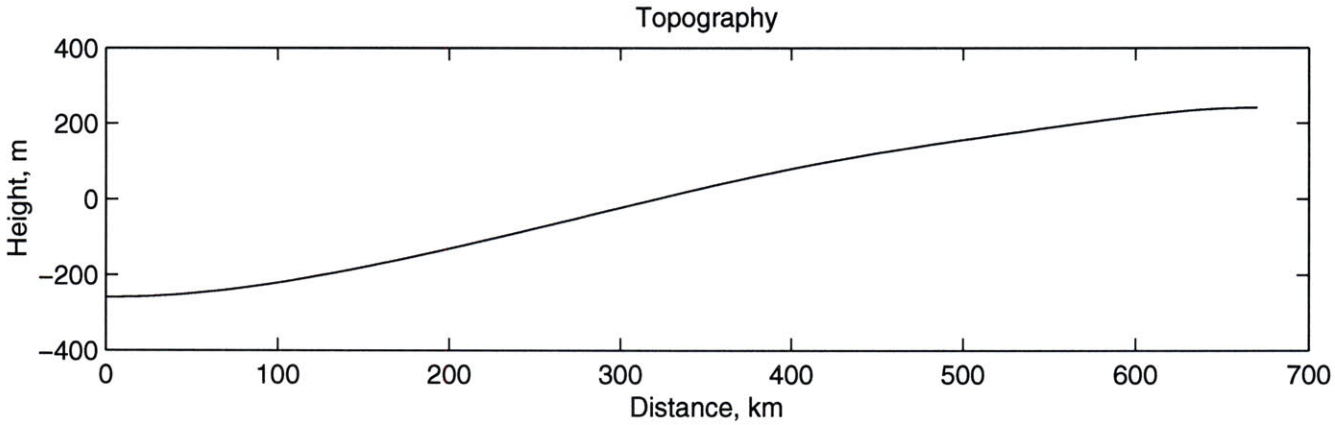

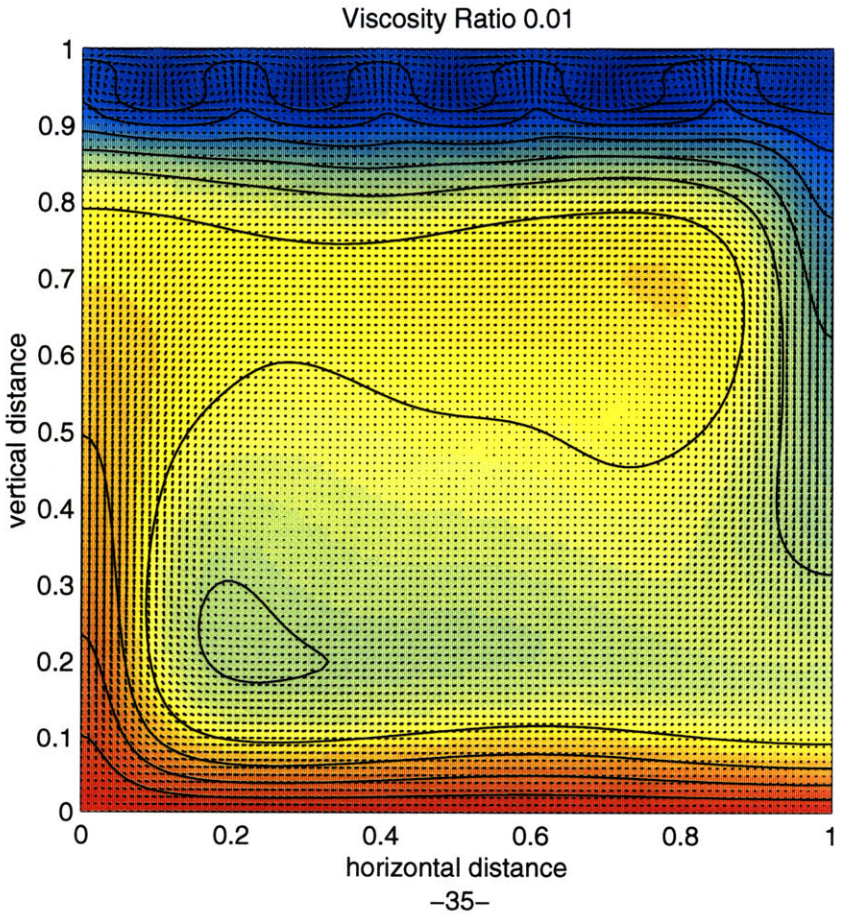

Figure #6 – Geoid

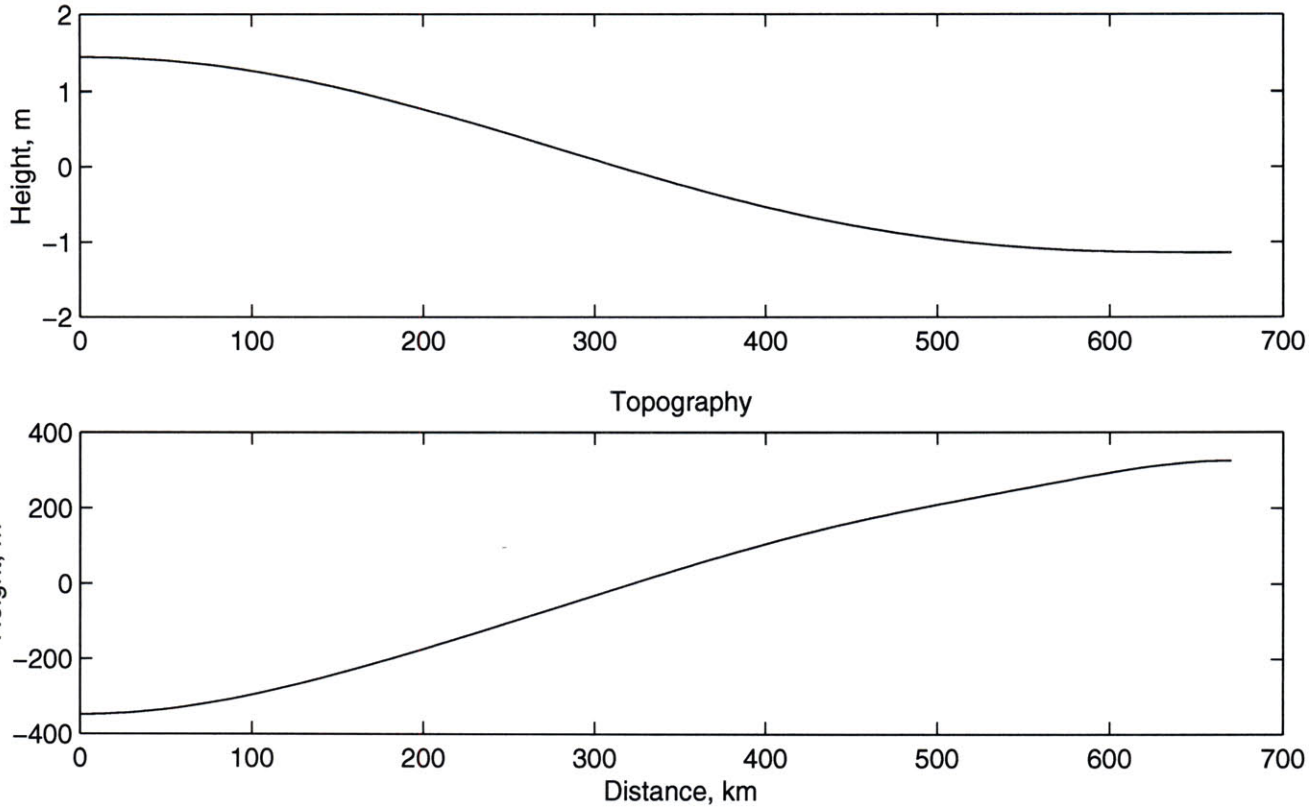

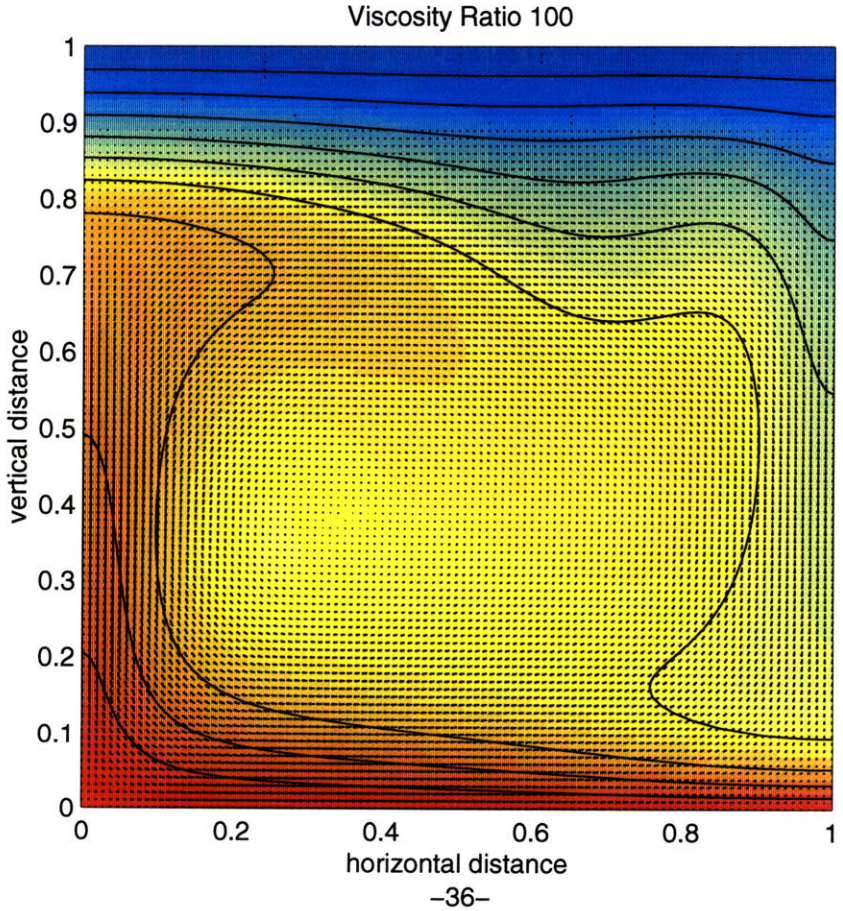

Figure #7 – Geoid

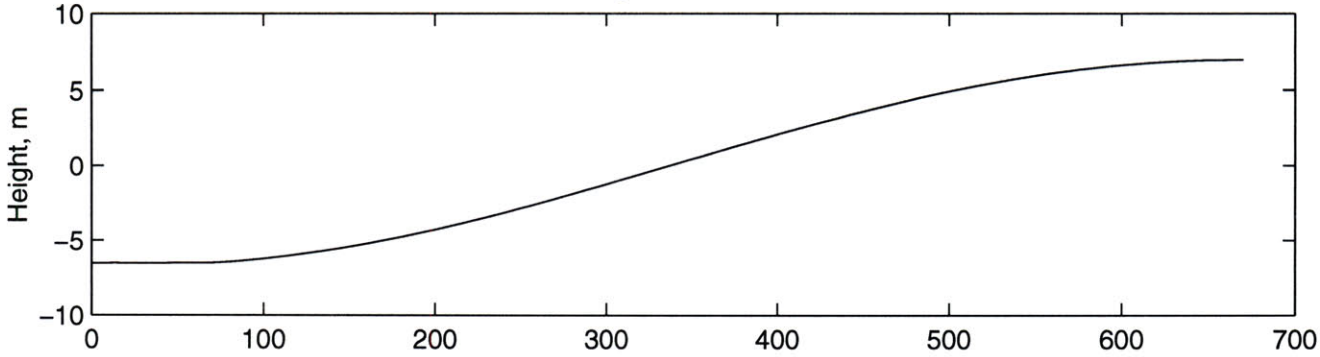

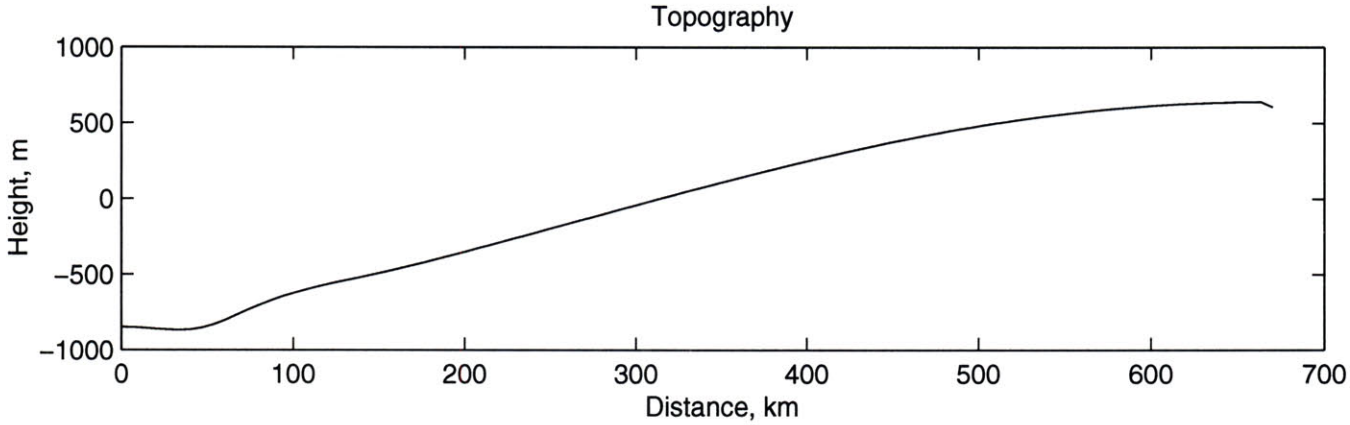

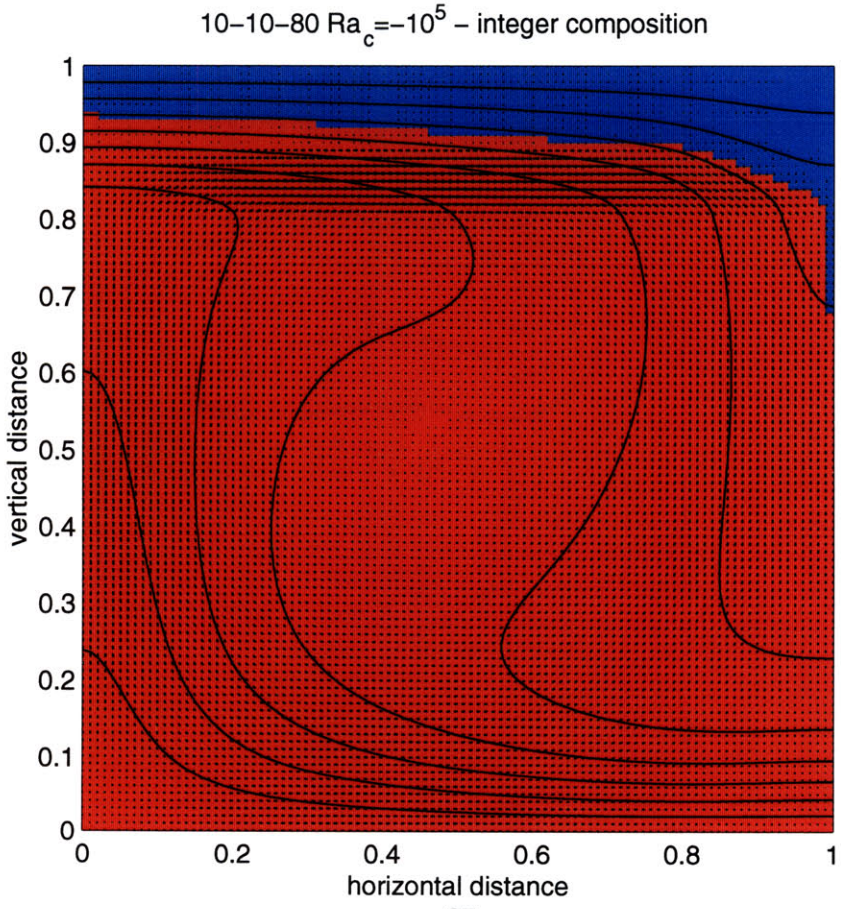

Figure #8 – Geoid

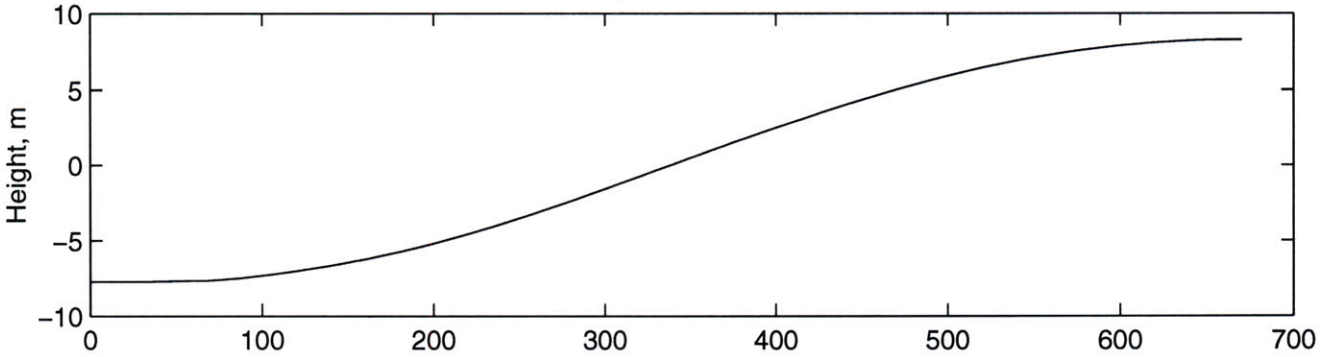

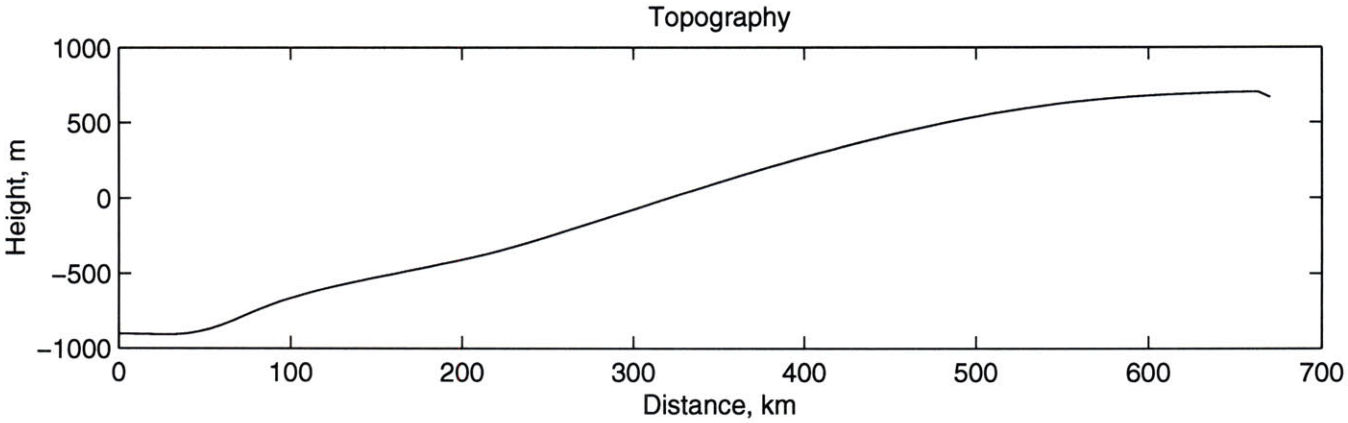

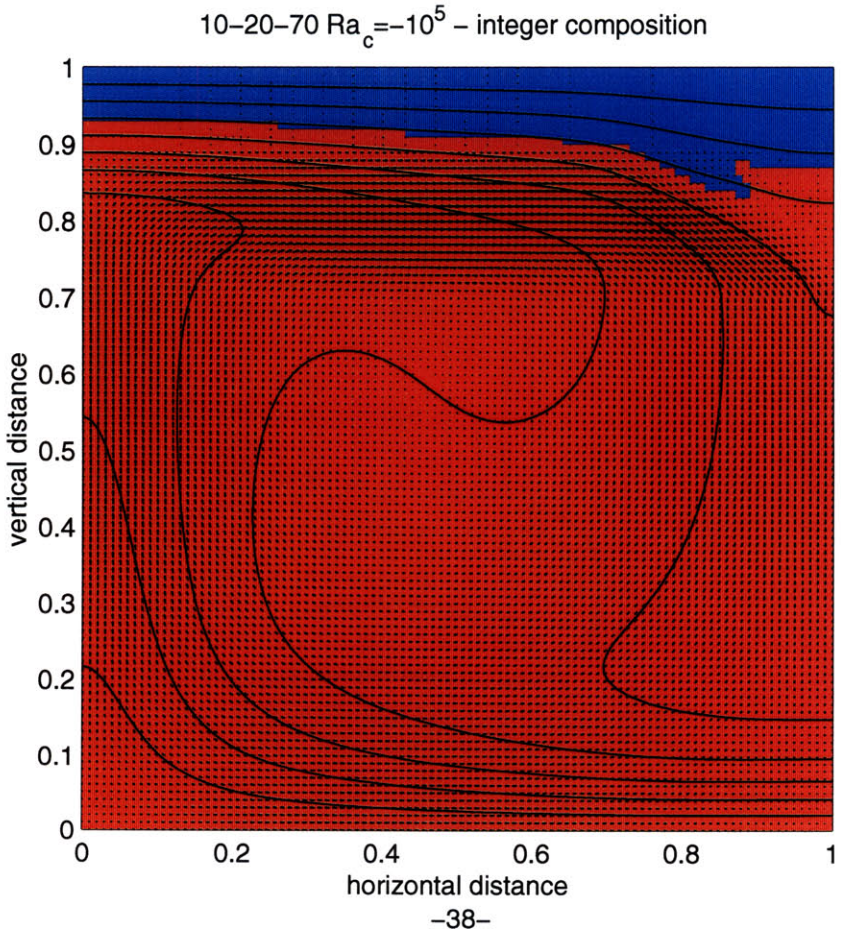

Figure #9 – Geoid

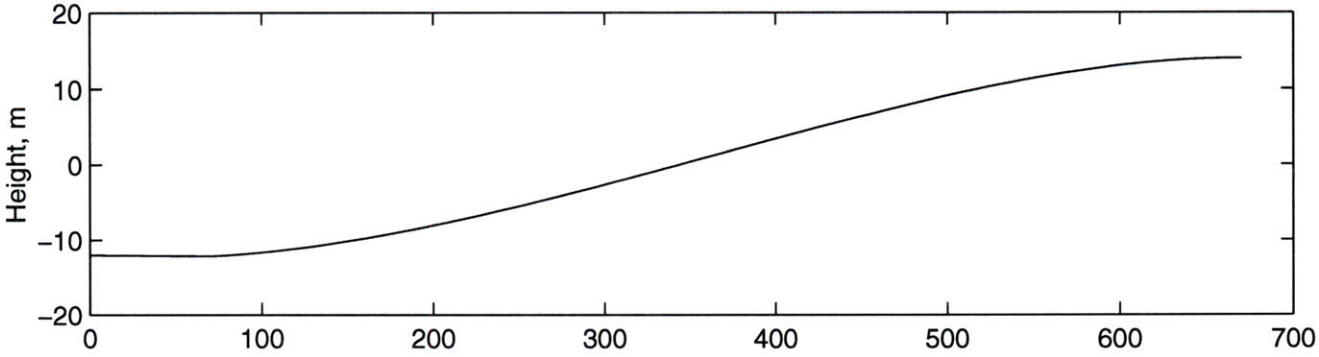

Topography

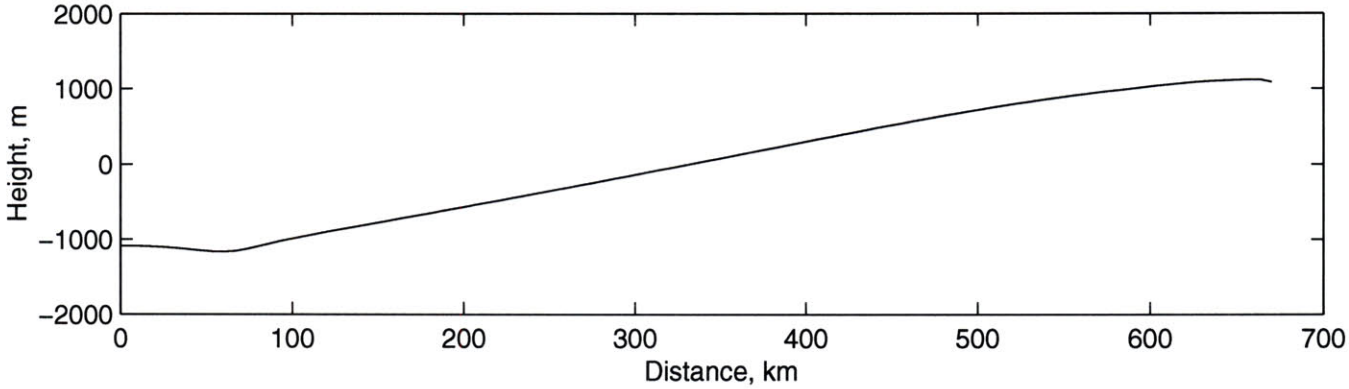

10–80–10 Ra_c=–10^5 – integer composition

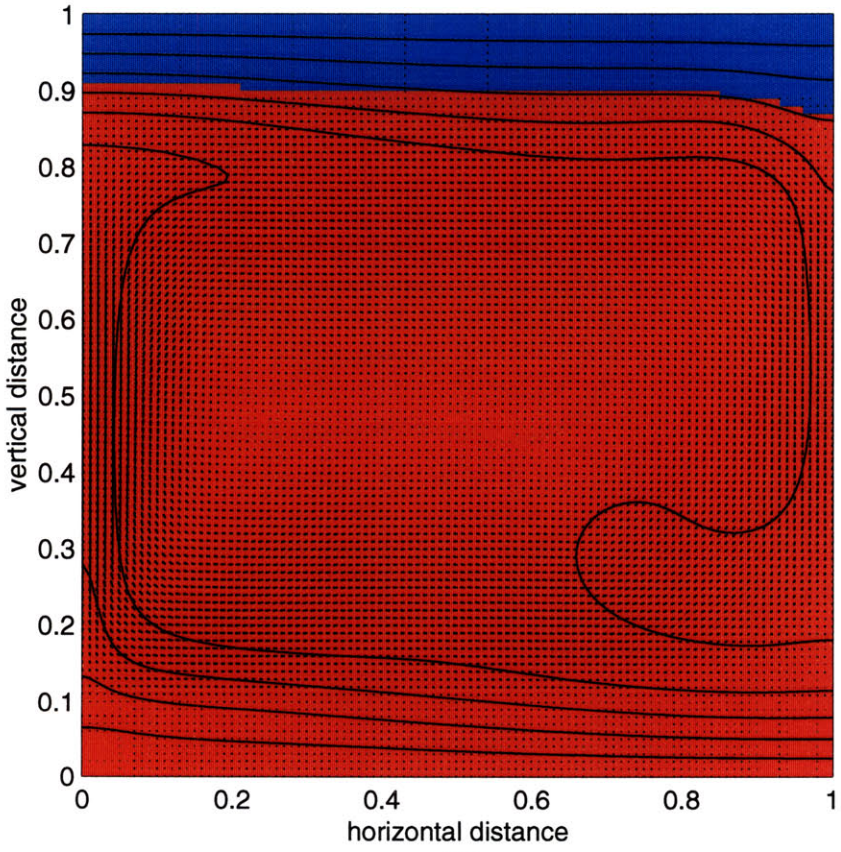

Figure #10 – Geoid

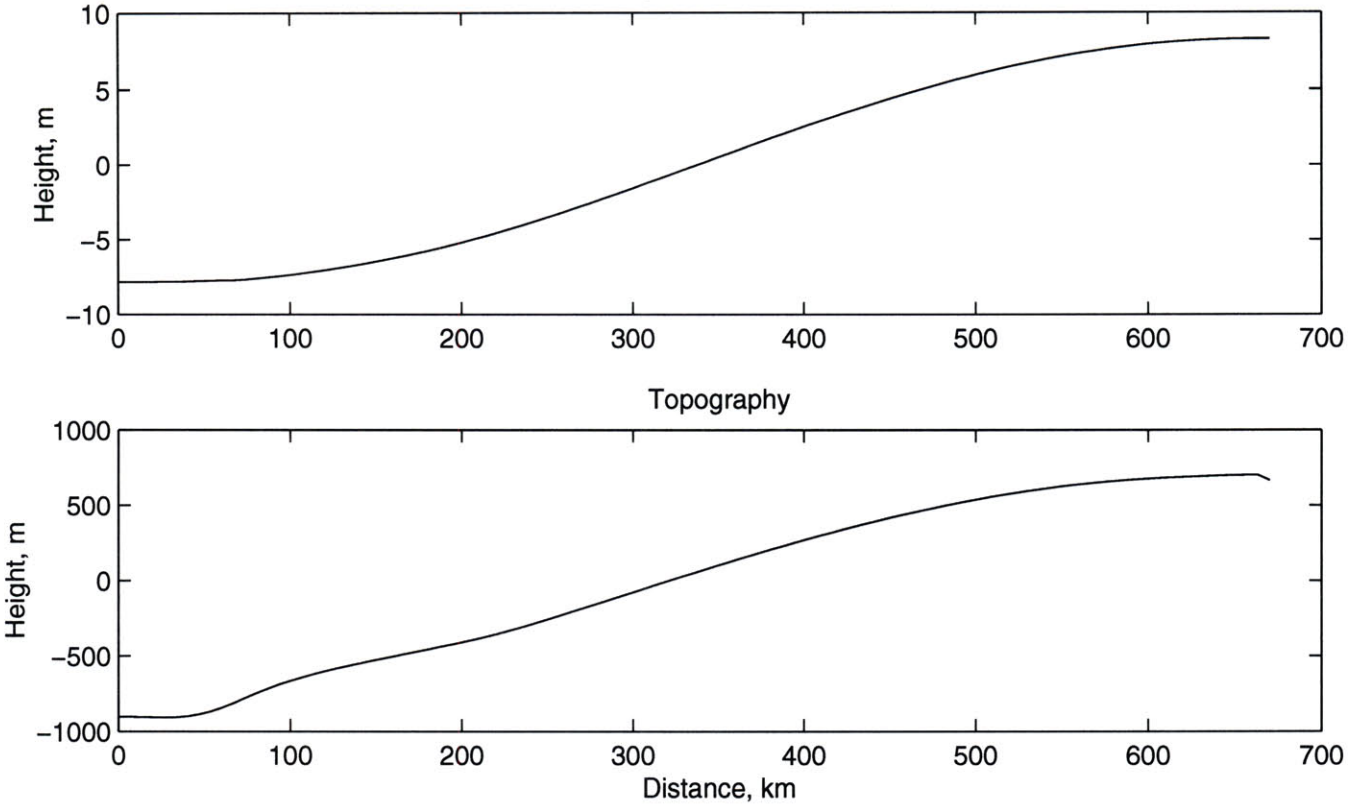

10–20–70 Ra_c=–10^5 – fractional composition

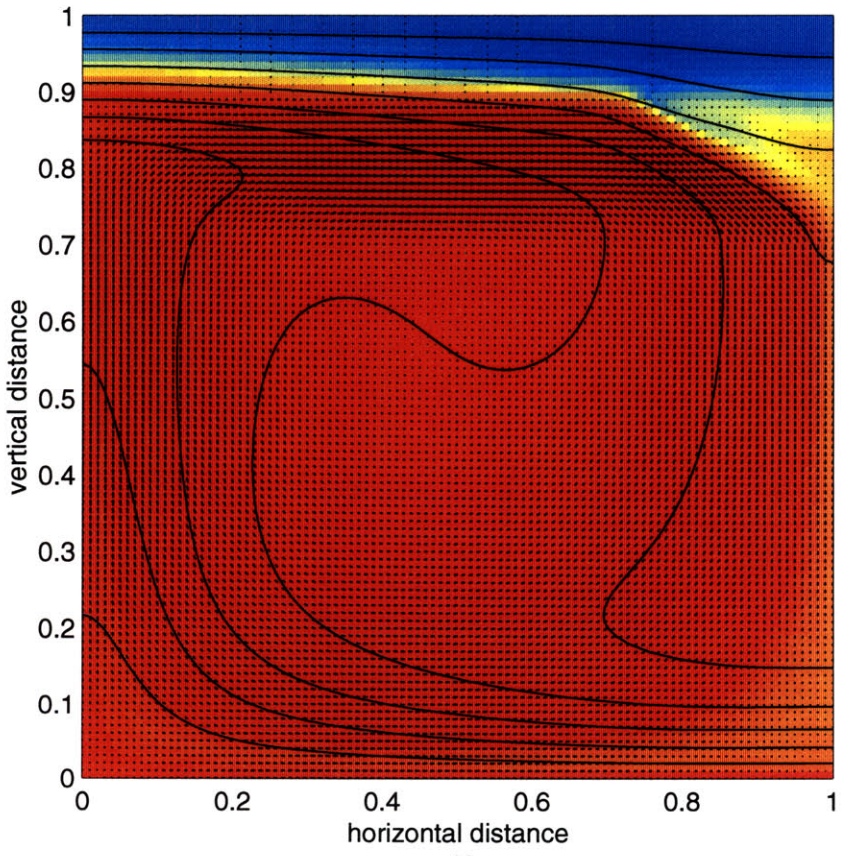

Figure #11 – Geoid

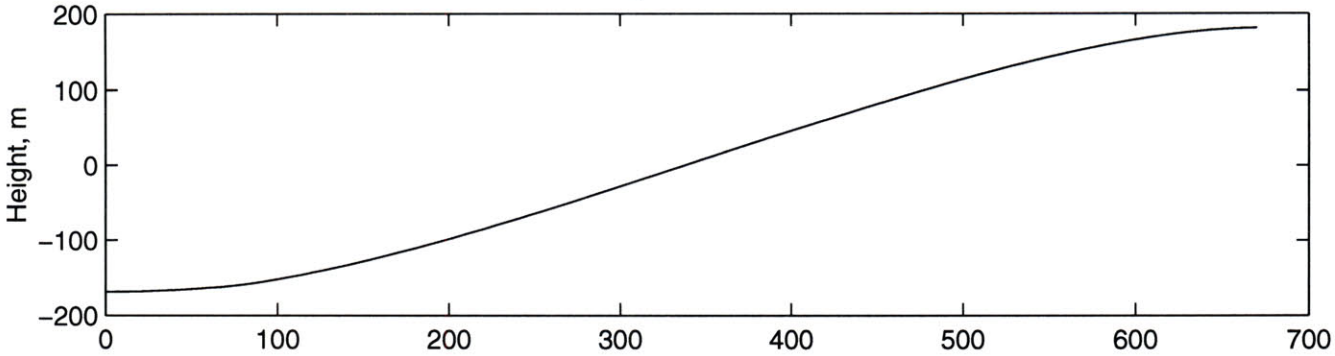

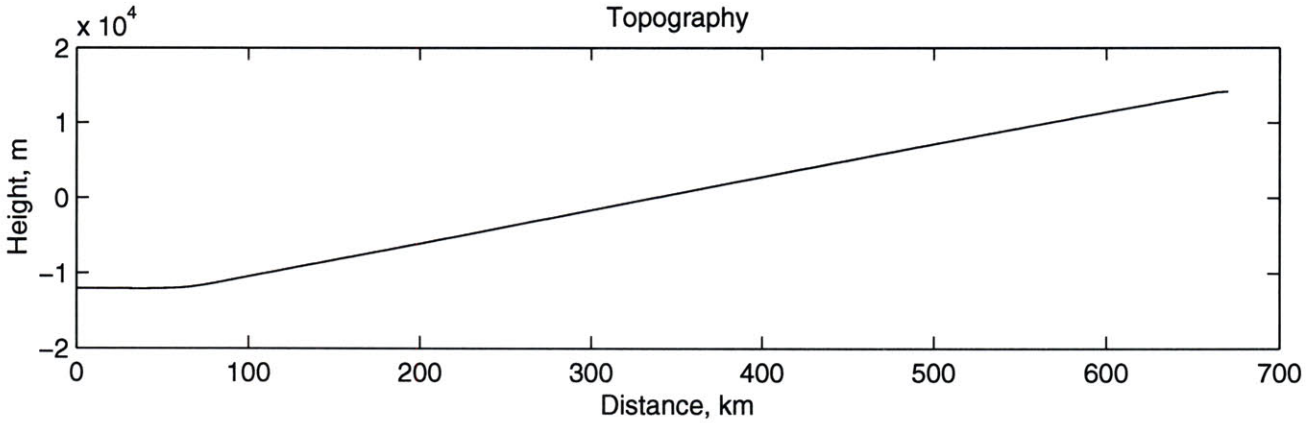

10–20–70 Ra_c=–5x10^5 – integer composition

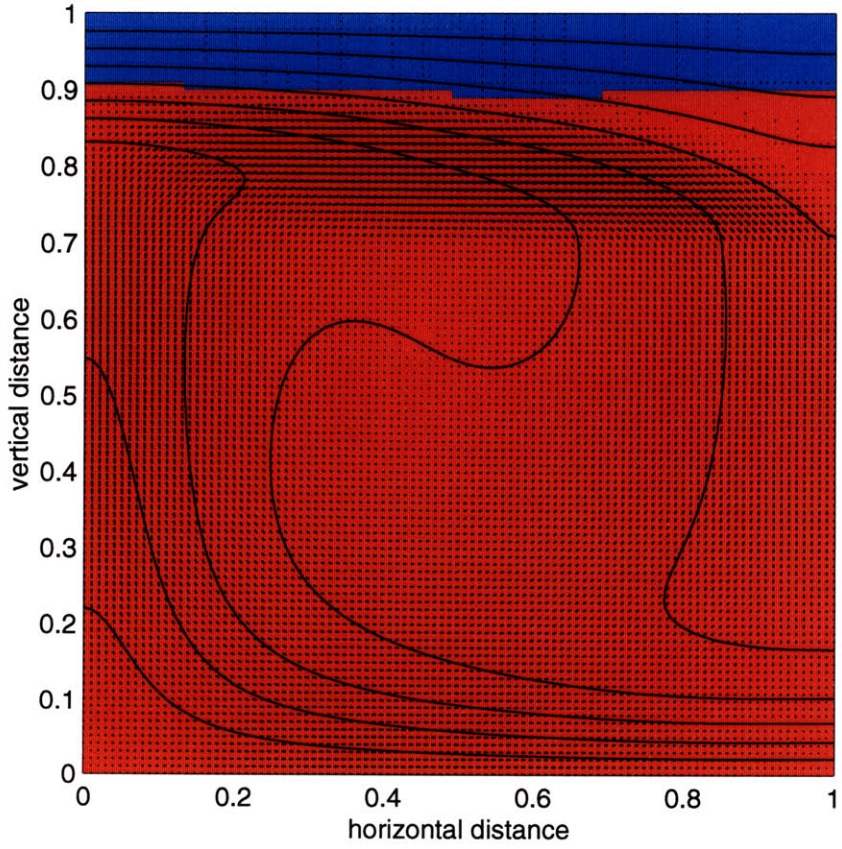

Figure #12 – Geoid

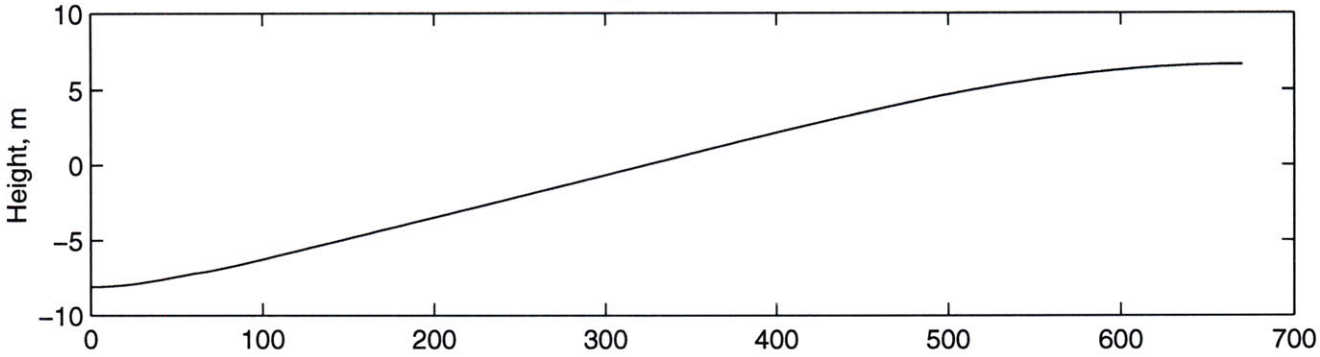

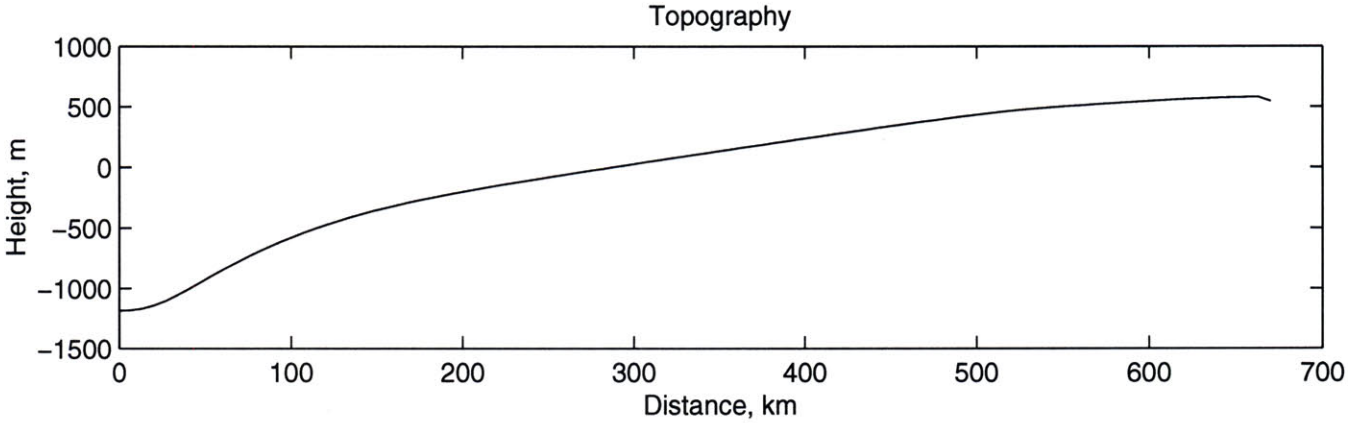

10–10–70–10 Ra_c=–10^5 – fractional composition

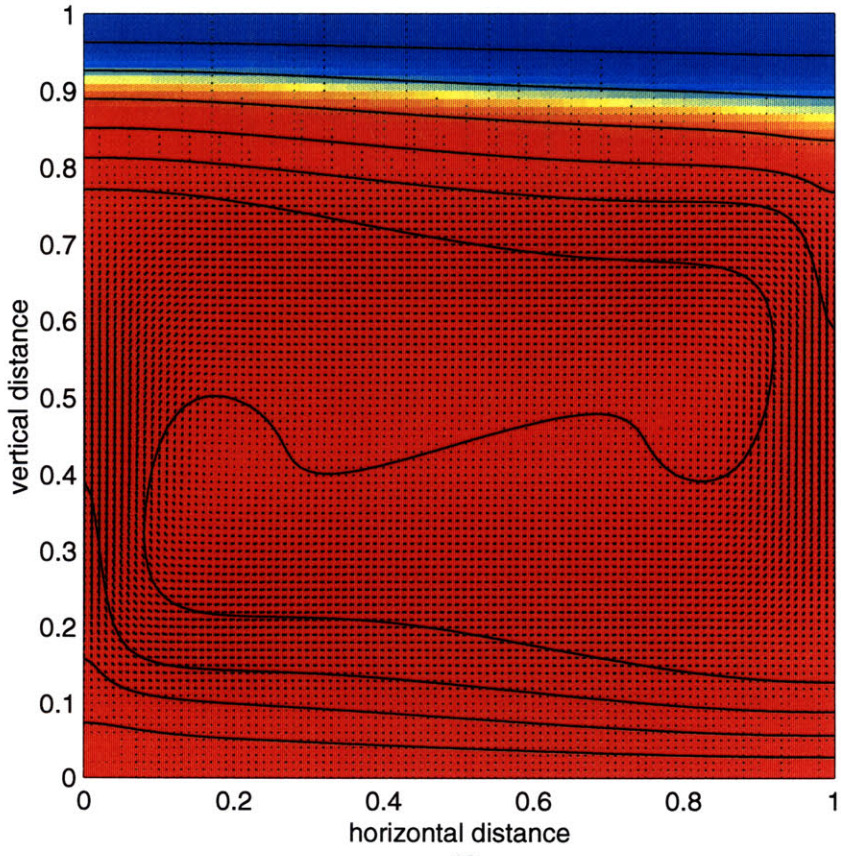

Figure #13 – Geoid

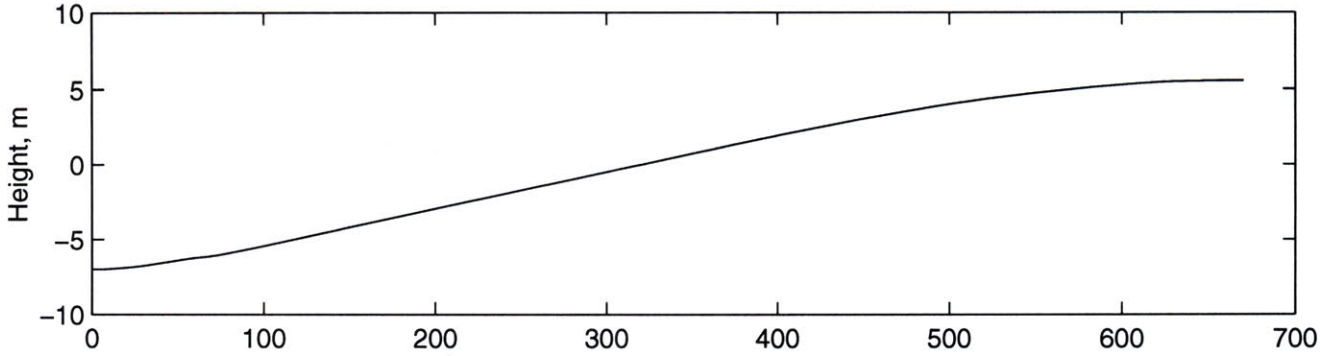

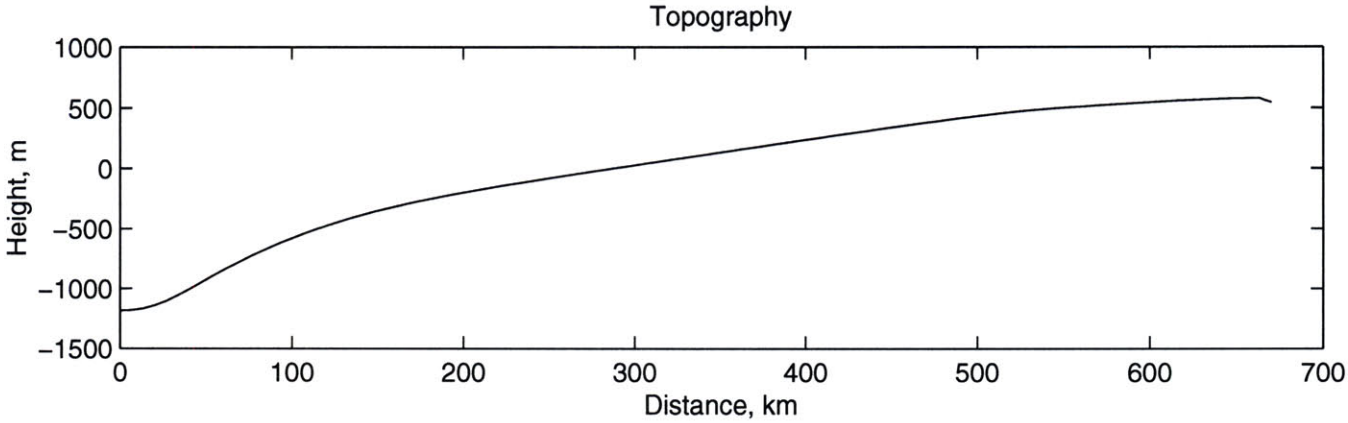

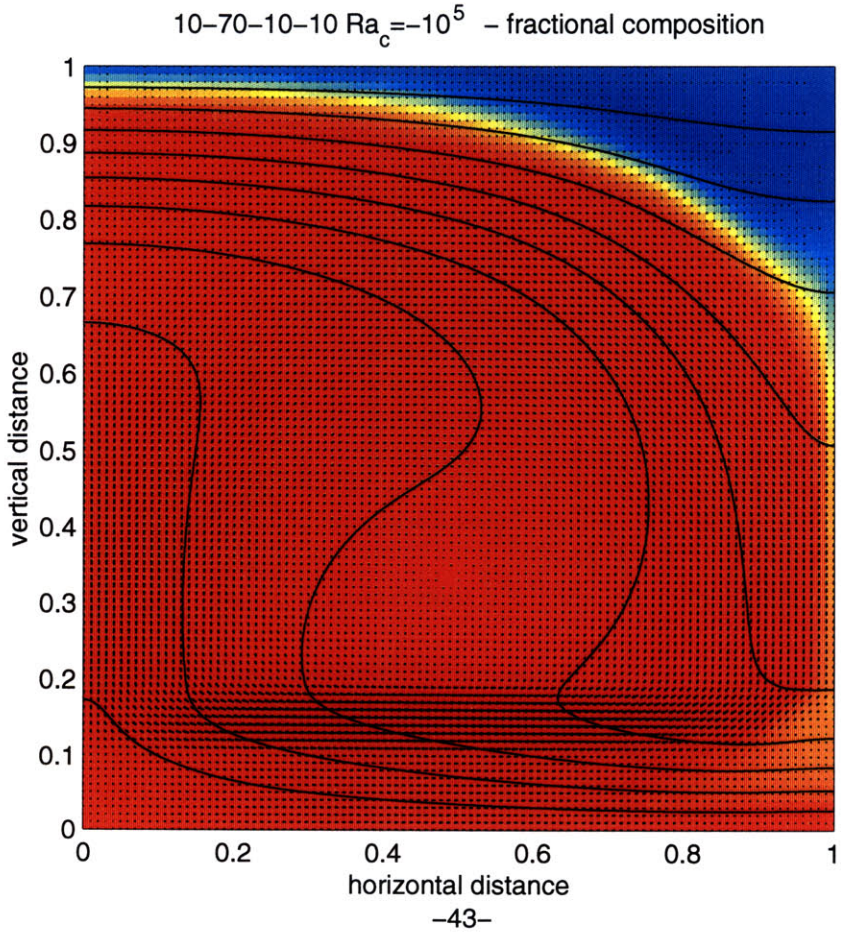

Figure #14 – Geoid

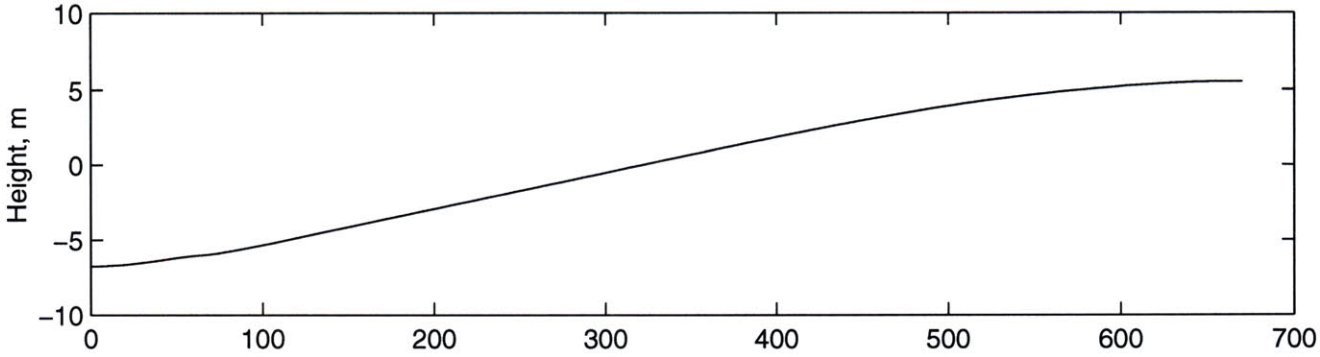

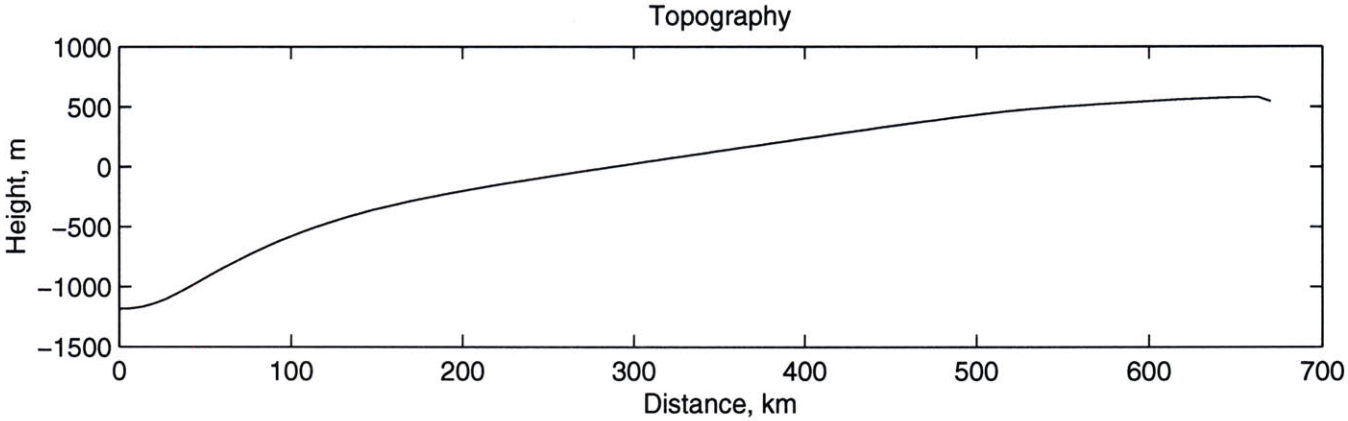

10–70–10–10 Ra_c=–10^5 – integer composition

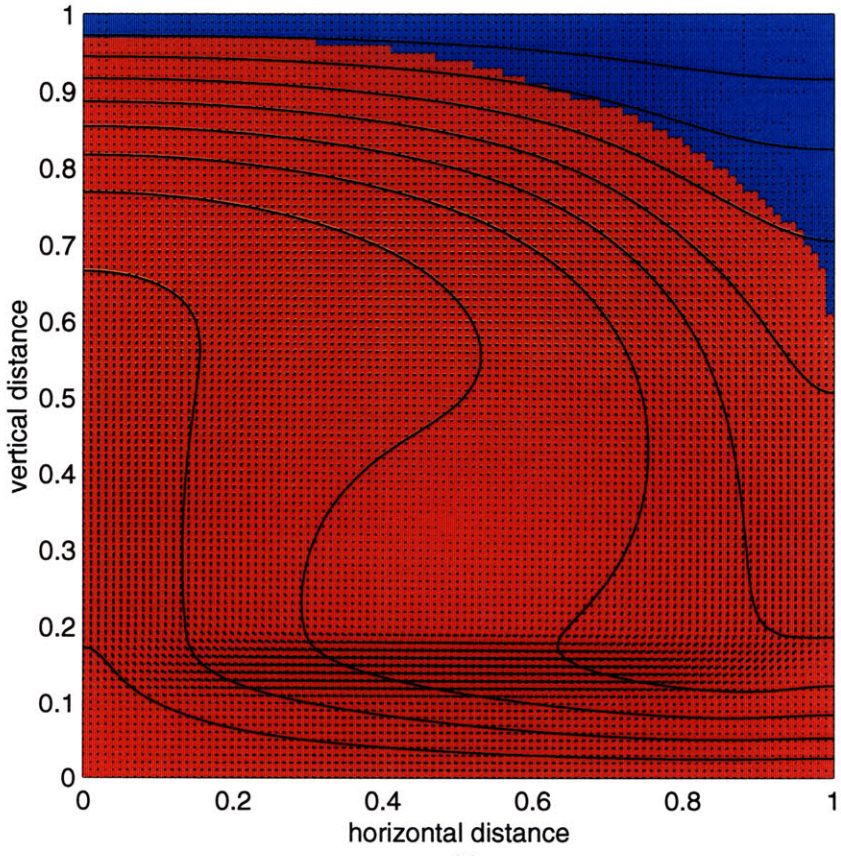

Figure #15 – Geoid

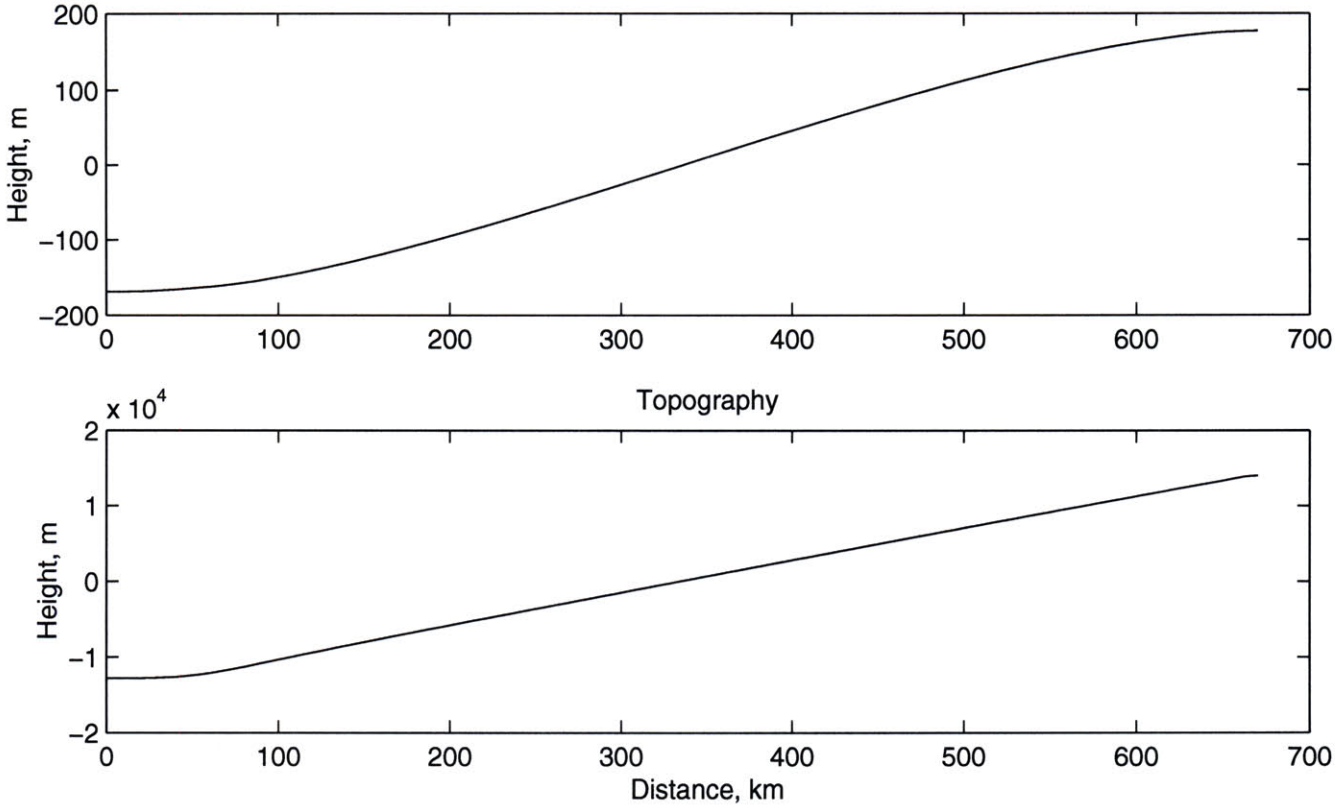

10–70–10–10 Ra_c=–5x10^5 – fractional composition

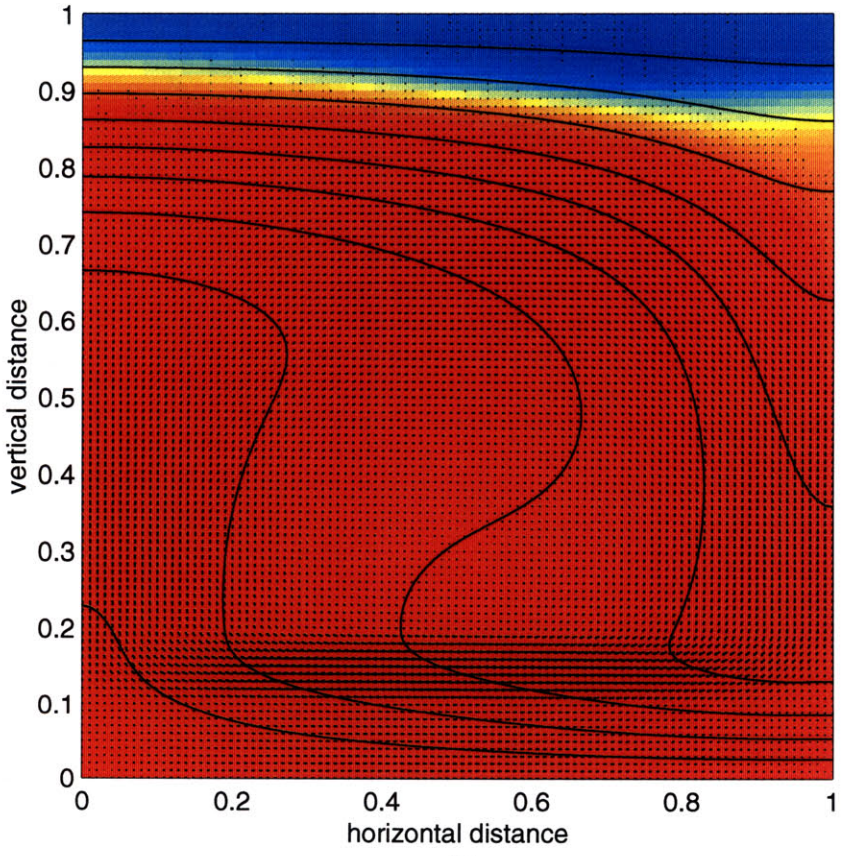

Figure #16 – Geoid Contributions, 10–20–70, $Ra_c=-10^5$

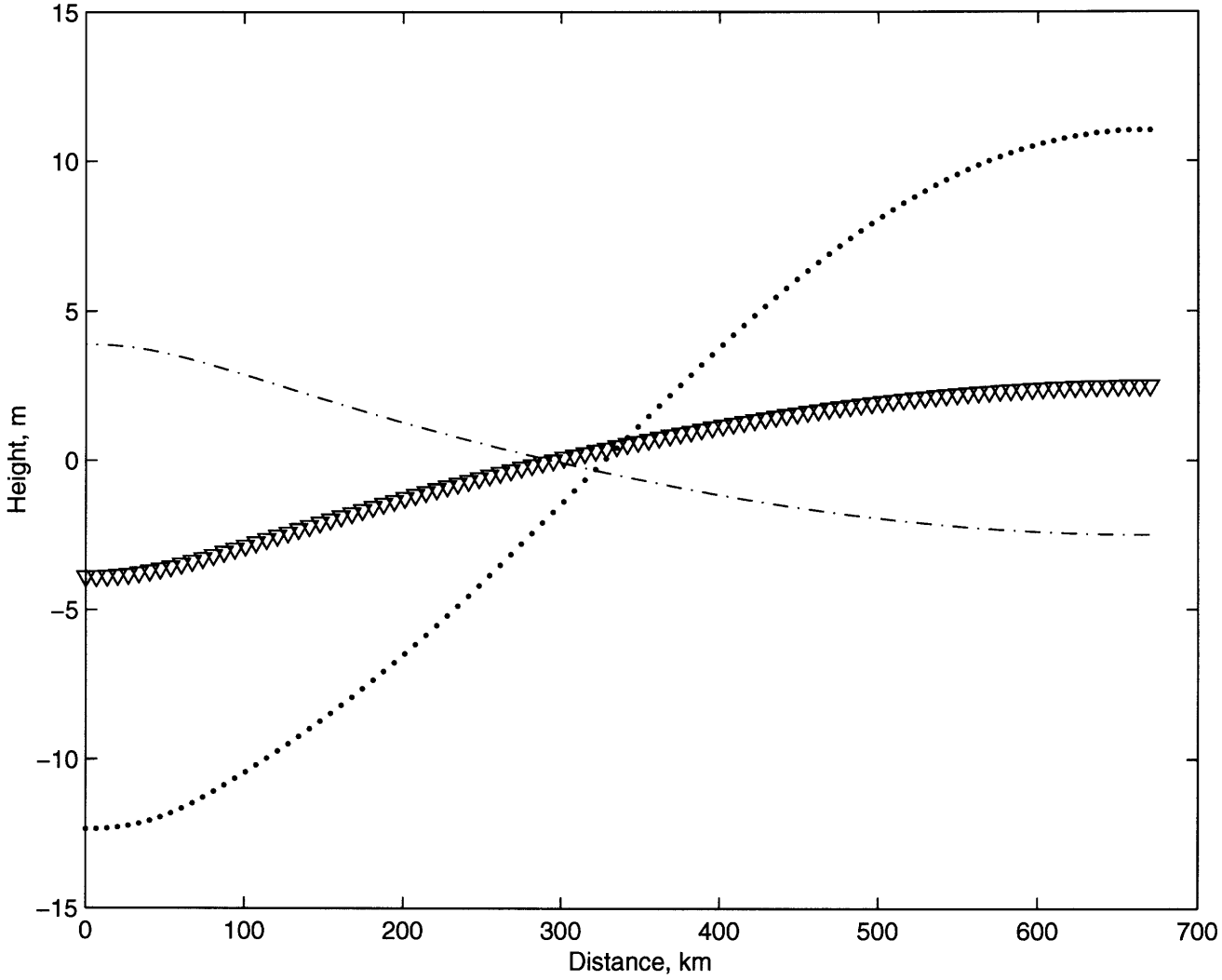

Acknowledgments

I would like to thank Brad Hager, Louise Kellogg, Clint Conrad, Katy Quinn, and Laurent Montesi for their many helpful discussions and answers on all matters pertaining to geophysics.

Without the assistance and hardware of the Adaptive Technology for Information and Computing laboratory, especially Jose Mercado and Kathy Cahill, I could never have finished this thesis. Thank you for helping me be "temporarily able" again.

I thank Elizabeth Agner, Jennie Hango, Avon Russell, and Jason Goodman for their open ears and willingness to offer good advice.

I am grateful to Rebecca Christianson for proofing this draft, and helping me stay sane until I could turn it in.

Every good thing to come out of this work is indebted to the selfless and kind efforts of Raymond Folse and Wes Lockwood.

I have no words to properly thank Denis Moskowitz for all of his support.

Finally, many thanks to Ron Canterna for giving me the opportunity, skills, and encouragement to begin this journey.